Politecnico di Torino

Politecnico di Torino

Master's degree in PHYSICS OF COMPLEX SYSTEMS

A.y. 2025/2026

Graduation Session March/April 2026

MHD stability of axisymmetric modes in tokamak fusion plasmas

Supervisor:
Professor Francesco Porcelli

Candidate:
Diletta Compagnone

Abstract

Nuclear fusion is the process that powers the stars and releases large amounts of energy. On Earth conditions to sustain fusion reactions in a plasma are difficult to obtain but still possible, and scientific research has put significant effort into achieving controlled fusion reactions, aiming at generating electricity. In this context, the functioning of tokamak reactors is pivotal to the advancement of the technology and to its future implementation on large scales. Though experimental results have been promising in the last years, much work still needs to be done before being able to fully understand the problems related to the stability of the plasma in these reactors. This thesis focuses on vertical, axisymmetric modes with toroidal mode number $n = 0$, which are of concern for the safe operation of tokamak plasma discharges, since these modes could grow uncontrolled and lead to vertical displacements of the plasma and plasma current disruptions. The work of this thesis aims at exploring the relation between the theoretical analysis and the numerical approach to simulation of tokamak plasmas. Numerical simulations were performed using the NIMROD code. A comparison between the linear theory and the numerical simulations of the axisymmetric modes $n = 0$ is presented, and the discussion is extended to the effects of nonlinearity on the simulated cases. A nonlinear analysis is necessary to verify whether linear equilibrium configurations may be driven unstable by perturbations of finite amplitude. Overall, the simulated cases show a close agreement with the theoretical dispersion relation, and small discrepancies are easily explained, whereas the nonlinear simulations need further investigation.

Acknowledgements

I would like to express my deepest gratitude to my supervisor, Prof. F. Porcelli, for his invaluable guidance. His wisdom and expertise have been a constant source of inspiration and have never ceased to amaze me throughout this work.

I also extend my sincere thanks to Dr. D. Banerjee, who mentored me as I navigated the challenging numerical aspects of this thesis.

I am profoundly grateful to my friends for their unwavering support. From the moments of doubt to those of celebration, I will never forget the journey we shared together.

Last but not least, I thank my parents for their unconditional love and for always believing in me.

Thank you all for having been part of this experience and of my life.

Table of Contents

List of Tables

List of Figures

Chapter 1

Introduction

By the end of the century, the demand for energy will have significantly increased under the combined pressure of multiple factors, such as population growth, increased urbanization and expanding access to electricity in developing countries. Growing electricity consumption comes from data centres, which are estimated to consume about 1.5% of the global electricity, growing at a 12% rate per year [1]. The rise of AI is accelerating the deployment of high-performance accelerated servers, leading to greater power consumption in data centres.

Fossil fuels have shaped the progress of civilization in the 19th and 20th century and these energy sources are still widely relied upon, at the great cost of greenhouse gases emissions and pollution. The world is experiencing an era of significant changes driven by the need to maintain and improve current living standards for a growing population while drastically reducing the carbon footprint of all human activities. In the strife of moving away from the direct use of fossil fuels, the role of the power sector is crucial and nuclear fusion, in particular, is believed to be able to ensure a sustainable, reliable, and affordable carbon free source of electricity.

Commercializing nuclear fusion is a technological challenge transcending mere scientific curiosity: great effort is put in accounting for social acceptance and economic feasibility of fusion power plants [2], and overall the joint action of the entire scientific community is required to make progress, which has led to some very interesting and promising results in the latest years.

1.1 Nuclear fusion

Fusion power plants would provide safe and clean electricity by exploiting the energy released during the process of nuclear fusion: light nuclei colliding at sufficiently high energy combine to form a larger nucleus.

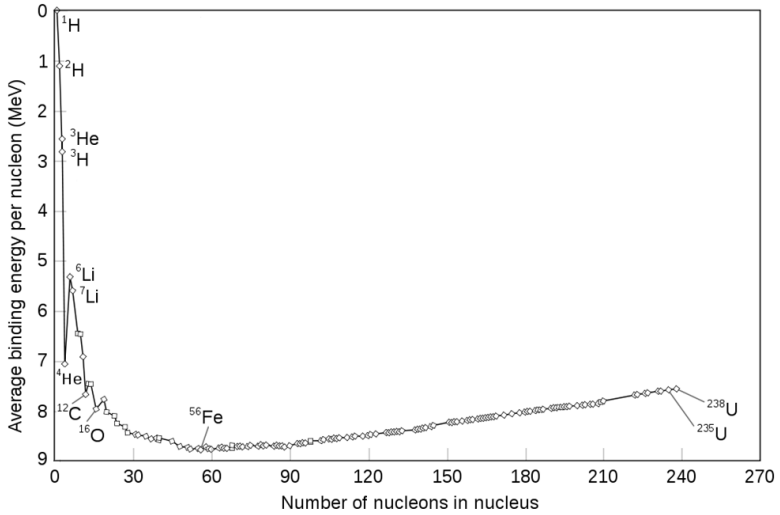

Figure 1.1: Binding energy per nucleon

In general, strong repulsive electrostatic forces between the positively charged nuclei prevent them from getting close enough for fusion to occur. However, if the conditions are such that the nuclei can overcome these electrostatic forces - at high temperatures, for instance - to the extent that they can come within a range of the order of 10^{-15} m, then the strong interaction acts as an attractive force on the nucleons. The amount of energy released by the formation of the heavier nucleus is determined by the difference in nuclear binding energy of the nuclei before and after the reaction - refer to Figure 1.1 -, and the consequent slight loss of mass during the process.

Contemporary fusion focuses on the reaction

$$ {}^{2}_{1}D \ + \ {}^{3}_{1}T \quad \rightarrow \quad {}^{4}_{2}He \ (3.5\text{MeV}) \ + \ {}^{1}_{0}n \ (14.1\text{MeV}) \tag{1.1} $$

between deuterium and tritium (D-T). Figure 1.2 depicts the cross-section[1] for various fusion reactions as a function of the energy of the center of mass. D-T

[1]The cross-section is defined as the probability that the process under study will take place in a collision between two particles

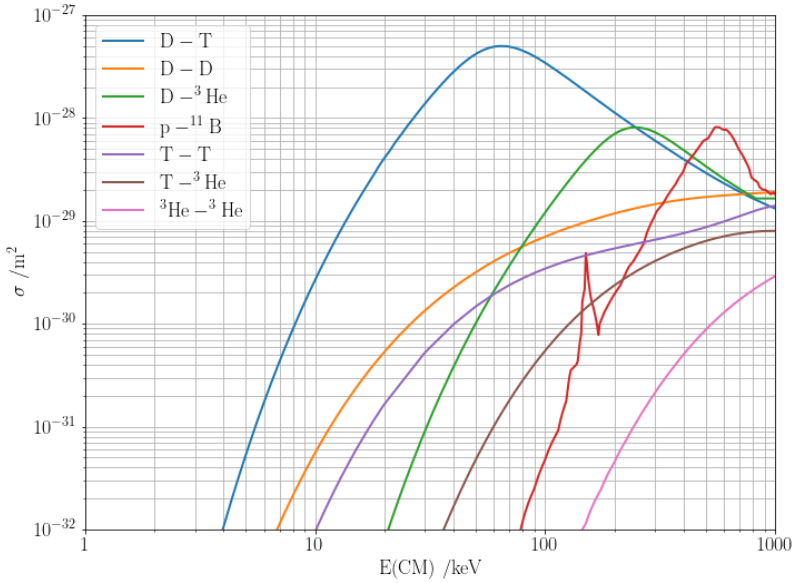

Figure 1.2: Fusion reaction cross sections as a function of the centre of mass energy. Data from the database of evaluated nuclear data (ENDF) of the International Atomic Energy Agency (IAEA).

reactions exhibit the highest cross-section at a lower temperature with respect to other reactions, thus offering a good compromise between the achievable cross-section and the experimentally obtainable temperature conditions.

Still, fusion fuel must be heated to extreme temperatures of the order of 10^8 K, and must be kept stable and confined for long enough to allow the nuclei to fuse. The aim of the controlled fusion research program is to achieve ignition, which occurs when enough fusion reactions take place for the process to become self-sustaining, with fresh fuel then being added to continue it.

A well-established condition is known as the Lawson criterion [3]. In the context of D-T reactions, the ${}^4_2He$ particles, often referred to as α particles, transfer their energy to the plasma, ensuring the self-sustaining high-temperature condition required for continuous thermonuclear burn. This process is important to maintain the energy balance:

$$\frac{dW}{dt} = P_{aux} + P_{\alpha} - P_{loss} \tag{1.2}$$

where

- $W \sim 3nT$ is the energy density of a plasma at temperature T and density

$n = n_{\text{electrons}} = n_{\text{ions}}$;

- P_{aux} is the auxiliary heating input power;
- $P_\alpha = n_D n_T \langle\sigma\nu\rangle \mathscr{E}_\alpha$ is the α particle heating power density, $\mathscr{E}_\alpha = 3.5MeV$, and $\langle\sigma\nu\rangle$ is the velocity averaged fusion reaction cross-section, which can be approximated with $c_0 T^2$ at a temperature between 10keV and 20 keV.
- P_{loss} collects all sources of energy loss by means of conducting, radiative, and convective phenomena. To quantify these losses, one can introduce the confinement time τ_E: $P_{loss} = W/\tau_E$

The criterion for ignition of the plasma is

$$P_\alpha \geq P_{loss} \quad \Longrightarrow \quad n\tau_E T > \frac{12}{\mathscr{E}_\alpha c_0} > 3 \cdot 10^{21} keV \cdot s \cdot m^{-3} \tag{1.3}$$

where $n\tau_E T$ is typically named fusion triple product.

In order to satisfy equation (1.3) in laboratory plasmas, research has developed two distinct experimental approaches to confine plasma.

One is inertial confinement fusion (ICF), which involves initiating the fusion reactions in small target fuel pellets, heated and compressed by high-power lasers. This type of reactions achieves very high densities ($\sim 10^{31} m^{-3}$) in very short confinement times ($\sim 10^{-11} s$).

The second experimental approach is magnetic confinement fusion (MCF), which exploits the response of charged particle to electromagnetic fields. A moving charged particle subject to the Lorentz force shows a gyrating motion characterized by a finite excursion - the Larmor radius - and by a frequency - the cyclotron frequency. Magnetic confinement devices are designed in such a way that plasma particles follow the helicoidal magnetic field lines preventing them from escaping or touching the walls of the device. In this context, one can define the parameter:

$$\beta = \frac{8\pi n k_B T}{B^2} \tag{1.4}$$

as the ratio between the plasma pressure and the magnetic pressure, which are the two opposing forces whose balance keeps the plasma contained. Good confinement happens for $\beta \ll 1$.

There is a variety of concepts for magnetic confinement fusion devices, but the majority of the effort focuses on the tokamak design.

1.2 Brief history of tokamaks

The term *tokamak* is an acronym for the russian words for *toroidal chamber with magnetic coils*, and the term was later adopted by other languages too. Tokamaks were first conceptualized by Soviet physicists A.D. Sakharov and I. E. Tamm in 1950, and experiments started in 1951 at Kurchatov Institute in Moscow, where the first device, T-1, began construction in 1958 [4]. This breakthrough in technology prompted the construction of other similar devices in the 1980s such as the Joint European Torus (JET) in Culham, United Kingdom, and the Tokamak Fusion Test Reactor (TFTR) at Princeton Plasma Physics Laboratory in the United States of America [5]. Many complementary devices and facilities around the world were also built to investigate the broad range of technological and engineering challenges. In the 1990s, JET and TFTR confirmed the physics of generating fusion energy using a mixture of tritium and deuterium. Both reactors developed understanding of alpha particles' role in heating fusion plasma, and JET set many magnetic confinement fusion power records - the latest of which in 2023 [6], shortly before its dismissal.

On this basis, research continued: machines demonstrated problems that limited their performance, and solving them would require a larger and more expensive machine, which is beyond the abilities of one country. The efforts of 34 nations culminated in the birth of the International Thermonuclear Experimental Reactor (ITER) project. The construction of ITER began in Cadarache, France in 2013, and tokamak assembly began in 2020 [7]. ITER's project is ambitious and still far from completion.

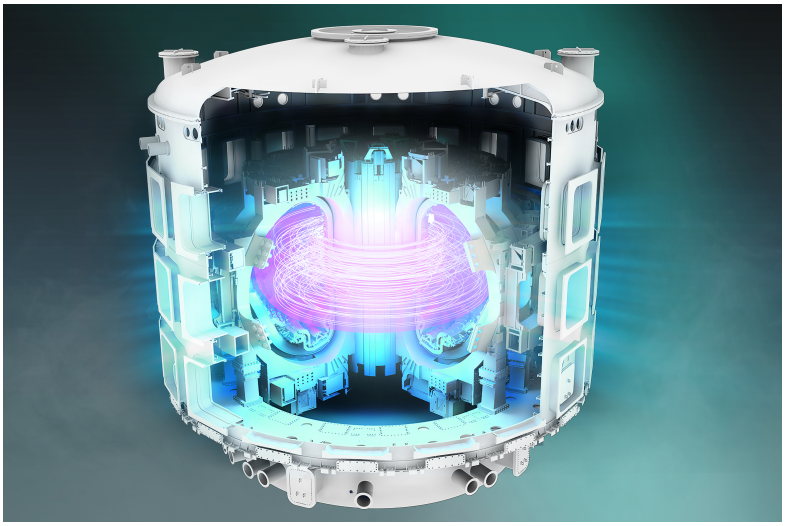

Figure 1.3: ITER tokamak design [7]

1.3 Alternatives to conventional tokamaks

For completeness, this section mentions some alternative designs to tokamaks, which have been proposed and tested during the past years.

Stellarator

In a stellarator the magnetic cage that confines the plasma is produced with a single coil system, which makes them suitable for continuous operation. Both magnet coils and plasma have a complicated shape, which, however, gives additional freedoms to optimize the performance. Wendelstein 7-X - Figure 1.4 - is an example of stellarator, built in Greifswald, Germany, by the Max Planck Institute for Plasma Physics (IPP).

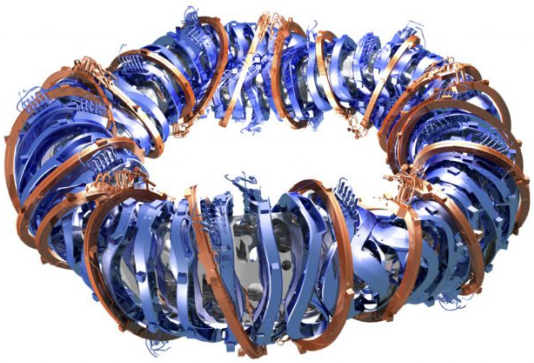

Figure 1.4: Wendelstein 7-X stellarator [8]

Spherical tokamak

Spherical tokamaks are characterized by a low aspect ratio, which makes the plasma shape almost spherical. The main advantage of this design is the possibility of operating at higher β values and thus lower magnetic fields. XuanLong-50 (EXL-50) is the first medium-size spherical torus in China [9], whereas MAST Upgrade is the largest operational spherical tokamak in and is located in Culham [10].

Compact tokamak

Another alternative to the conventional design is the compact tokamak, characterized by smaller dimensions with respect to their conventional counterpart. To

be able to keep this smaller size, compact tokamaks in general make use of much stronger magnetic field components. IGNITOR is one example of this design: conceptualized in the late 1970s [11], it aimed ad demonstrating ignition in a magnetically confined plasma [12]. Shorter confinement times to reach ignition can be obtained, according to equation 1.3, with higher densities, and density of the plasma in a tokamak scales as B/R, thus benefiting from the small dimensions and the high magnetic field. Another project which followed the same high-magnetic field tokamak reasearch line is SPARC, which was developed by the MIT Plasma Science and Fusion Center [13].

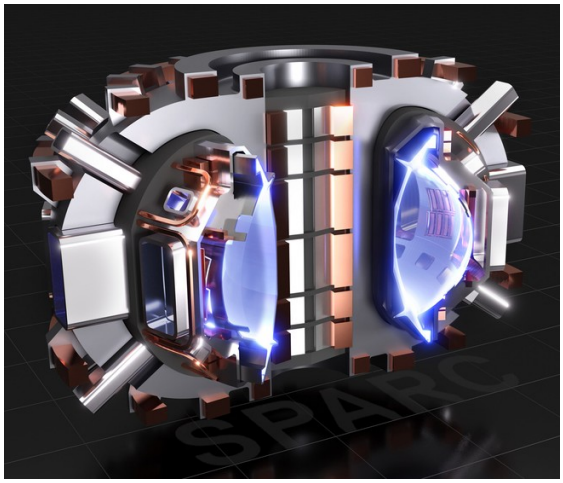

Figure 1.5: SPARC tokamak [14]

1.4 Problems associated to plasma shaping in tokamaks

The section of tokamaks chambers is not circular: plasma shaping is associated with magnetic divertors and with reducing the problem of plasma-wall interaction. Though helping with some issues, elongated plasmas are problematic as they are prone to certain types of instabilities, initiated by an axisymmetric perturbation, leading to vertical displacements events (VDEs). In these phenomena, the plasma shifts vertically and may touch the vacuum chamber, resulting in plasma current disruptions and possible damage to the mechanical structure of the tokamak device. For this reason, uncontrolled VDEs must be avoided, and study of this phenomena is needed.

Recently, a certain type of $n = 0$ mode [2] was studied. It has been named vertical displacement oscillatory mode (VDOM) and it has been proposed that it might be driven unstable by resonant interaction with fast ion orbits [15]. VDOMs are oscillatory solutions to the dispersion relation for vertical displacement normal modes with a discrete frequency of oscillation, and they are the main focus of this thesis.

1.5 Thesis work and structure

This thesis aims at presenting a theoretical overview of the VDOM dispersion relation as a preamble to numerical simulations of tokamak plasmas perturbed by finite amplitude, vertical initial shifts. A comparison between the theoretical model analysis and the numerical approach is presented. Results from simulations of the axisymmetric modes, performed using the NIMROD code, will be shown and analyzed. Lastly the need for a nonlinear analysis of the model will be justified and results of nonlinear simulations will be reported.

Aside from this introduction, the thesis is structured as follows:

- Chapter 2 - Plasma Physics and Theory of Tokamak Plasmas
  This chapter is dedicated to an insight in plasma physics. A definition of plasma is given, followed by a theoretical description of plasma dynamics. Ideal MHD is explained, as it constitutes the basis for deriving the dispersion relation which will later be useful to the discussion. A description of tokamak devices components is provided. The VDOM dispersion relation is derived through a heuristic model, and compared to the same relation obtained from a more accurate mathematical derivation.
- Chapter 3 - NIMROD MHD simulations
  This chapter aims at providing an overview of the NIMROD code and of the numerical simulations set-up.
- Chapter 4 - Linear and nonlinear numerical results
  This chapter is dedicated to presenting the simulations performed for this

[2] Here, the n=0 mode represents an instability in the tokamak with toroidal mode number equal to zero. Toroidal (n) and poloidal (m) mode numbers define the spatial structure of plasma oscillations in tokamaks. They represent the number of full wavelenghts along the toroidal and poloidal directions around the torus. The toroidal mode number n indicates the number of twists around the torus. The poloidal number m indicates the number of intersections a magnetic field line makes with a cross section. Perturbations are generally proportional to a term of the type: $e^{i(m\theta - n\varphi)}$, where θ and φ represent the poloidal and toroidal angles, respectively.

thesis. The first section contains the linear simulations results. Differences and similarities to the theoretical model are highlighted. The driven oscillator perturbation method is then discussed and used to explore specific details. The last section is dedicated to the discussion on nonlinearity, simulations are shown and results explained.

- Chapter 5 - Conclusions

Chapter 2

Plasma physics and theory of tokamak plasmas

2.1 Definition of plasma

Plasma is often described as the fourth state of matter. Matter spontaneously reaches this state when at thermodynamic equilibrium at $T \geq 10^4$ K, that is when the thermal oscillations of the particles are sufficiently high in energy to ionize a gas. Equivalently, there need to be external agents, such as photons, whose energy is greater than the minimum ionization energies of the atoms in the gas. In an ionized gas, atoms separate in electrons and nuclei and the presence of these charged, free particles drastically changes the behaviour of matter. Long-range Coulomb forces become non negligible and if the number of interactive particles in the system is big enough, a collective behaviour is observed, replacing Brownian motion and random thermal agitation. The particles in the system start to behave according to an average electromagnetic field in consequently orderly motions.

One could say that: a plasma is defined as a ionized gas, electrically quasi-neutral, dominated by a collective behaviour. Let us briefly analyze each of these characteristics:

- The degree of ionization of a gas at thermodynamic equilibrium is measured by the Saha equation:

$$\frac{n_i}{n_n} \propto \frac{T^{\frac{3}{2}}}{n_i} e^{\frac{-U_i}{k_b T}} \tag{2.1}$$

  where n_i and n_n are the number of ionized particles and of neutral particles, respectively, and U_i is the atomic ionization energy. In Figure 2.1, one can

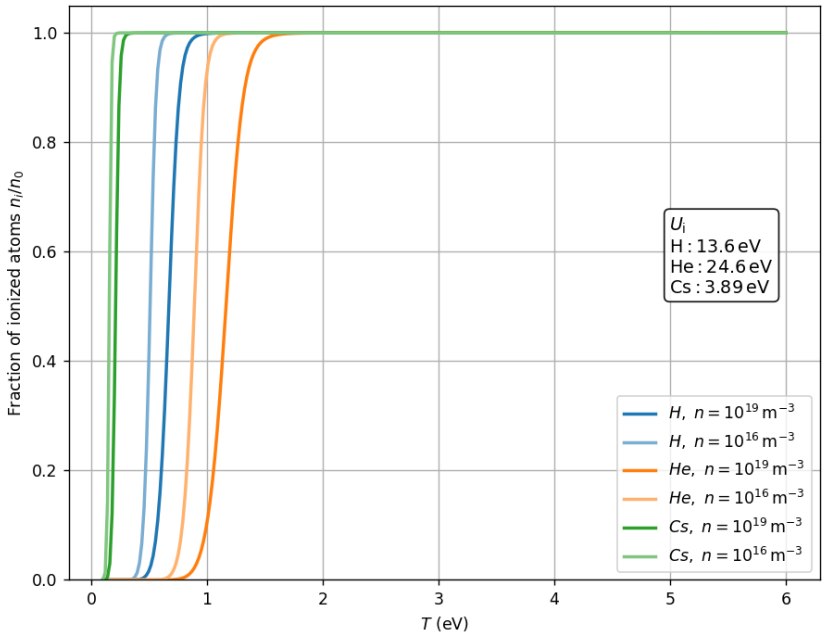

Figure 2.1: Degree of ionization according to the Saha equation

find a visual representation of this relation. The degree of ionization becomes non neglible when $k_B T \lesssim U_i$.

- Assume to introduce in a plasma a fixed charge Q. Electrons and ions in the plasma change their distribution in space in such a way that the additional charge is shielded over a distance $\lambda_D = \left(\frac{T}{4\pi n e^2}\right)^{1/2}$. This distance is the Debye length. This is the concept of quasi-neutrality and it makes sense if the number of particles within the Debye sphere, $\frac{4\pi}{3}\lambda_D^3 n$ is large. Then, one can define the plasma parameter:

$$g = (n\lambda_D)^{-1} \tag{2.2}$$

and the condition:

$$g \ll 1 \tag{2.3}$$

is taken as the defining criterion for a plasma.

- Criterion 2.3 implies that inter-particle collisions are relatively weak. It follows that, in this regime, collective behaviour dominates over individual particle behaviour. Coulomb collisions are weak and the plasma can be well approximated by a perfect gas: the charged particles move under the average electric and magnetic field, self-consistently generated by the particle motion

itself, undisturbed by particle collisions. In the limit $g \to 0$, the plasma behaves as a perfect gas. In tokamak plasmas, the typical value of g is of the order 10^{-7}.

2.2 Mathematical description of a plasma

Consider a full ionized plasma, made up by N particles, with $N \gg 1$. We can write an equation of motion for each particle in the system:

$$m_i \frac{d^2\vec{r}_i}{dt^2} = q_i \left[\vec{E}(\vec{r},t) + \frac{1}{c}\frac{d\vec{r}_i}{dt} \times \vec{B}(\vec{r},t) \right] \qquad i = 1, 2, ..., N \tag{2.4}$$

Additionally, consider:

$$\rho_{q,pl}(\vec{r},t) = \frac{\sum_{\Delta V} q_i}{\Delta V} \quad \text{plasma charge density} \tag{2.5}$$

$$\vec{J}_{pl}(\vec{r},t) = \frac{\sum_{\Delta V} \dot{\vec{r}}_i q_i}{\Delta V} \quad \text{plasma current density} \tag{2.6}$$

where the summations extend to all particles in an elemental volume $\Delta V(\vec{r})$ centered in $\vec{r}$. In the presence of external charges and currents, the total charge density and current density are respectively $\rho_q(\vec{r},t) = \rho_{q,pl} + \rho_{q,ext}$ and $\vec{J}(\vec{r},t) = \vec{J}_{pl} + \vec{J}_{\text{ext}}$. Lastly, consider the Maxwell equations:

$$\begin{cases} \nabla \cdot \vec{E} = 4\pi\rho_q \\ \nabla \times \vec{B} = \frac{4\pi}{c}\vec{J} + \frac{1}{c}\frac{\partial \vec{E}}{\partial t} \\ \nabla \cdot \vec{B} = 0 \\ \nabla \times \vec{E} = -\frac{1}{c}\frac{\partial \vec{B}}{\partial t} \end{cases} \tag{2.7}$$

We have a system of (8+3N) equations for (8+3N) variables $(\phi, \vec{A}, \rho_q, \vec{J}, \vec{r}_i)$, where ϕ and $\vec{A}$ represent the scalar and vector potential of the electric and magnetic fields.

Due to the large value of N it is not convenient to solve this set of equations, and it is preferable to move to a statistical description. Indeed we can define, in a phase space $(\vec{r}, \vec{v})$, a distribution function $f(\vec{r}, \vec{v}, t)$ and its moments:

- density: $n(\vec{r},t) = \int f(\vec{r},\vec{v},t) d^3v$
- charge density: $\rho_q(\vec{r},t) = \sum_j q_j \int f_j(\vec{r},\vec{v},t) d^3v \quad , j = e, i$

- average fluid velocity: $\vec{u}(\vec{r},t) = \frac{1}{n(\vec{r},t)} \int f(\vec{r},\vec{v},t)\vec{v}d^3v$
- current density: $\vec{J}(\vec{r},t) = \sum_j q_j \int f_j(\vec{r},\vec{v},t)\vec{v}d^3v \quad , \quad j = e,i$

where $j = e,i$ meant we are considering a plasma made of electrons and one positive-ion species.

It is then possible to write the Boltzmann equation:

$$\frac{\partial f_j}{\partial t} + \vec{v}\cdot\nabla f_j + \frac{q_j}{m_j}\left(\vec{E} + \frac{1}{c}\vec{v}\times\vec{B}\right)\cdot\frac{\partial f_j}{\partial \vec{v}} = \left(\frac{\partial f_j}{\partial t}\right)_{\text{coll}} \tag{2.8}$$

where $\left(\frac{\partial f_j}{\partial t}\right)_{\text{coll}}$ is the collisional term. And coupling it to the Maxwell equations and

$$\rho_q(\vec{r},t) = \sum_j q_j \int f_j d^3\vec{v} + \rho_{\text{q, ext}} \tag{2.9}$$

$$\vec{J}(\vec{r},t) = \sum_j q_j \int f_j \vec{v} d^3\vec{v} + \vec{J}_{\text{ext}} \tag{2.10}$$

we get the Maxwell-Boltzmann plasma description, a system of 10 equations for 10 variables $(\phi, \vec{A}, \rho_q, \vec{J}, f_j)$.

At local thermodynamic equilibrium, the distribution function corresponds to the Maxwellian distribution:

$$f_M(\vec{r},\vec{v},t) = \left[\frac{m}{2\pi T(\vec{r},t)}\right]^{\frac{3}{2}} n(\vec{r},t) e^{-\frac{m}{2T(\vec{r},t)}[\vec{v}-\vec{u}(\vec{r},t)]^2} \tag{2.11}$$

2.3 Magnetohydrodynamics

A plasma is a complex system exhibiting long range interactions and unlike systems which are dominated by nearest-neighbour collisions, the behaviour of a plasma is strongly influenced by macroscopic electric and magnetic fields. In tokamak plasmas, these collective phenomena have the potential to perturb the equilibrium magnetic configuration, giving rise to large scale instabilities that impact significant portions of the plasma column. To describe these instabilities, it is necessary to leave local descriptions and treat the plasma like a continuous fluid of charged particles.

Magnetohydrodynamics (MHD) is the theory describing the behaviour of electrically conducting fluids. Most of the work in MHD deals with magnetostatic configurations, since conducting fluids are often confined by strong magnetic fields

for long times compared to typical flow decay times. The effects of fluid dynamics is thus weak and give rise to quasi-static magnetic field configurations.

Define the convective derivative $d/dt = \partial/\partial t + \vec{v} \cdot \nabla$. Equations that make up the ideal MHD model, in Gaussian (c.g.s.) units, are:

- the continuity equation, representing the conservation of mass in the system:

$$\frac{\partial \rho}{\partial t} + \nabla \cdot (\rho \vec{v}) = 0 \tag{2.12}$$

- the force balance, which accounts for the inertial force, the thermal pressure force [1], and the Lorentz force:

$$\rho \frac{d}{dt} \vec{v} = -\nabla p + \frac{1}{c} \vec{J} \times \vec{B} \tag{2.13}$$

  The force due to the gravitational potential is negligible in the case of laboratory plasmas.

- Ampere's law:

$$\nabla \times \vec{B} = \frac{4\pi}{c} \vec{J} \tag{2.14}$$

  where the displacement current is neglected because of the nonrelativistic limit.

- Faraday's law:

$$\nabla \times \vec{E} + \frac{1}{c} \frac{\partial \vec{B}}{\partial t} = 0 \tag{2.15}$$

- Ohm's law:

$$\vec{E} + \frac{1}{c} \vec{v} \times \vec{B} = 0 \tag{2.16}$$

- the equation of state, for which we assume adiabatic transformations [2]:

$$\frac{d}{dt} \left(\frac{p}{\rho^{\Gamma}} \right) = 0 \tag{2.17}$$

  where $\Gamma = c_p/c_v$ is the ratio of specific heats.

[1] Conditions close to thermodynamic equilibrium are assumed, implying an isotropic pressure tensor.

[2] Variations in the thermodynamic state happen sufficiently fast and on sufficiently large spatial scales that dissipation effects such as heat conduction can be neglected, thus justifying considering the system as adiabatic.

In static equilibrium, when $\vec{v} = 0$, equation 2.13 describes the balance between pressure and magnetic force, maintaining the plasma confinement.

This set of equations contains seven independent variables: three velocity components, density, pressure and two magnetic fields components ($\nabla \cdot \vec{B} = 0$).

2.4 Reduced ideal MHD model

It is possible to reduce the number of independent variables of the MHD model in the case of incompressibility: $\nabla \cdot \vec{v} = 0$. Consider a plasma column subject to a strong magnetic field in the axial direction: $\vec{B} = \nabla\psi \times \hat{e}_z + B_z\hat{e}_z$, where the flux function ψ is introduced as equal to the axial component of the vector potential. Strong local gradients can be generated only on the poloidal plane and the z-coordinate becomes ignorable ($\partial/\partial z = 0$). Expressing the velocity as $\vec{v} = \nabla\phi \times \hat{e}_z + v_z\hat{e}_z$, where ϕ represents the stream function, and introducing the vorticity vector $\vec{\omega} = \nabla \times \vec{v} = \nabla^2\phi\hat{e}_z + \nabla v_z \times \hat{e}_z$, and the quantity $U = \nabla^2\phi$, after some calculations - Ref.[16] - and the proper normalization, the equations of the reduced-MHD model are:

$$\frac{\partial\psi}{\partial t} + [\phi, \psi] = 0 \tag{2.18}$$

$$\frac{\partial}{\partial t}\nabla \cdot (\rho\nabla\phi) + \left[\rho, (\nabla\phi)^2\right] + [\phi, \rho]\, U + \rho\,[\phi, U] = [\psi, J] \tag{2.19}$$

where $J = -\nabla^2\psi$ and the brackets $[\chi, \zeta] = \hat{e}_z \cdot \nabla\chi \times \nabla\zeta$ were introduced.

The reduced ideal-MHD model does not contain the full range of solutions of the MHD physics.

2.5 Tokamak reactor

This section consists of a brief overview of the most important features in a tokamak reactor. This section mostly refers to the ITER tokamak design, even though most features are common to other reactors too.

2.5.1 Vacuum vessel

One of the main components of a tokamak is the toroidal vacuum vessel, within which the plasma is confined in such a way that it does not touch the vessel walls. The chamber provides a high-vacuum environment and acts as the primary confinement barrier for radioactivity. Cooling water circulates through the vessel's

double walls and the vessel itself provides support for internal components such as the blanket and the divertor.

Blanket modules cover the inner walls of the vacuum chamber protecting the structure from heat and slowing down high-energy neutrons produced by the fusion reactions. In ITER, part of the project consists in replacing some blanket modules in specialized modules to test for tritium breeding.

The divertor is situated at the bottom of the vacuum vessels and extracts heat and ash produces by the fusion reaction. Its purpose is to minimize plasma contamination and protecting the surronding walls from thermal and neutronic loads. Its function will be discussed in a later section in more detail.

2.5.2 Magnets and magnetic fields in a tokamak

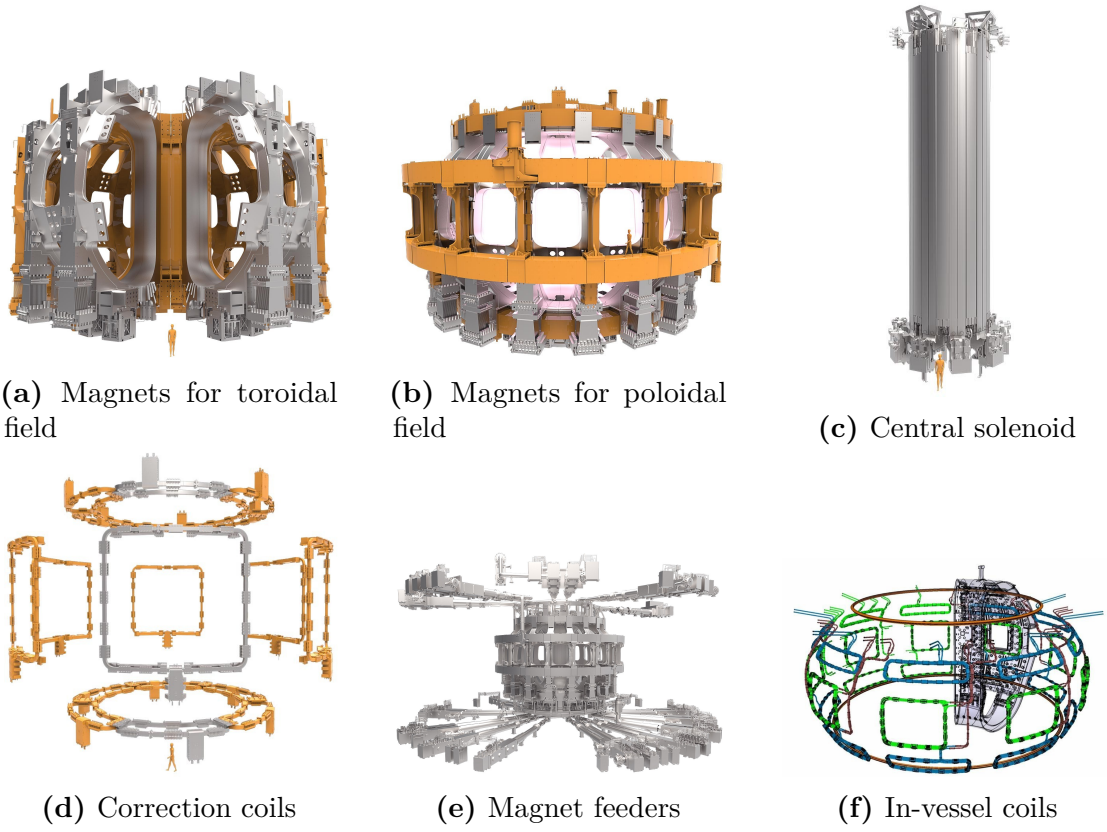

(a) Magnets for toroidal field

(b) Magnets for poloidal field

(c) Central solenoid

(d) Correction coils

(e) Magnet feeders

(f) In-vessel coils

Figure 2.2: ITER magnets components schematics [7]

To be able to confine the plasma, tokamak devices make use of a complex set of magnets:

- Toroidal field magnets, Figure 2.2a, wind around the vacuum vessel in a solenoid fashion and produce a toroidal magnetic field whose primary function is to confine plasma particles. Their structure is critical, and any misalignment results in errors of the magnetic configuration.
- The poloidal component of the magnetic field is produced by a toroidal current carried by the plasma itself, playing the role the secondary transformer circuit. The primary transformer circuit is an inner set of coils, constituting the central solenoid, Figure 2.2c.
- Additional poloidal field coils, Figure 2.2b, are situated outside of the toroidal field magnet structures and contribute to shape the plasma, to keep it in position to assure its stability.
- Figure 2.2d shows the correction coils, which are inserted to compensate for field errors caused by geometrical deviations and assembly tolerances.
- Figure 2.2e represents the magnet feeders, which connect the magnets to their power supplies, and convey and regulate the cryogenic liquids needed to cool and control the temperature of the magnets.
- Non-superconducting in-vessel coils, Figure 2.2f, provide additional control on the plasma.
- Additional magnets are required for the divertor.

Magnets used in tokamaks are usually made from superconducting alloys - in ITER, Nb_3Sn (niobium-tin) or Nb-Ti (niobium-titanium) - which need to be cooled at temperatures of a few Kelvin degrees. Superconductors are able to carry higher thresholds of electrical currents and to produce stronger magnetic fields at a cheaper operation cost.

2.6 Plasma elongation

Early tokamak experiments, such as TFTR, had circular cross sections, as these were easier to understand and design. Research in 1980s contributed to the understanding that non-circular cross sections could improve stability and performance.

External current-carrying coils can be added to the tokamak and by driving enough current in them, one can establish a divertor configuration: one or more magnetic X-points are produced. A divertor X-point is defined as a point in space in which the poloidal field has zero magnitude. In a tokamak, because of the toroidal

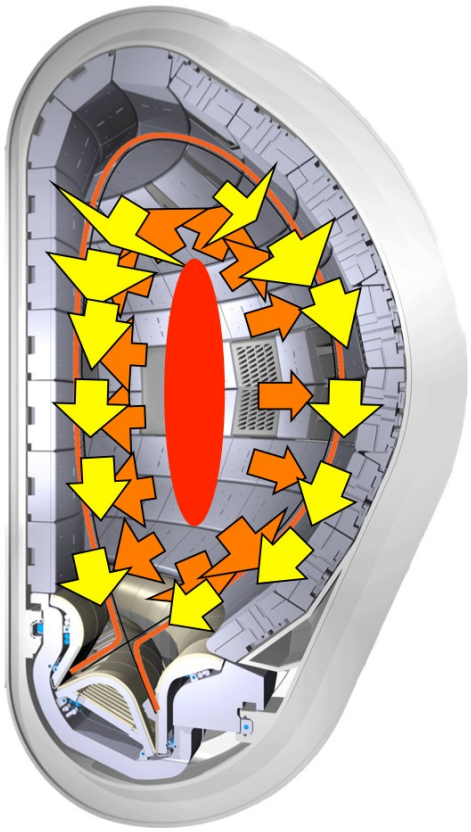

Figure 2.3: DTT cross section [17] - divertor configuration

geometry, the X-point is a magnetic X-line that closes on itself after one toroidal revolution. The magnetic flux surface intersecting the X-point is called separatrix and defines the last closed flux surface.

In tokamaks operating without the divertor configuration, the last closed surface is established by inserting a material limiter facing the plasma on the inner wall of the vacuum chamber. This limiter is in contact with the plasma and particles escaping the last closed flux surface may damage the wall and other plasma-facing components. This problem is solved by the divertor: the plasma edge is uncoupled from the vessel walls, meaning that exhaust heat and escaping plasma particles are diverted towards a known region of the vessel, located near the X-point and called the divertor chamber.

If up-down symmetry is maintained, two X-points belonging to the same separatrix are produced on opposite sides of the plasma. In most modern cases, the preferred configuration is a single null magnetic divertor with only one divertor chamber located below the plasma - Figure 2.3. Examples of this configuration are tokamaks

like JET or DTT [3].

Plasma shaping and elongation are closely related to the problem of vertical plasma stability. Elongation is produced by external currents pulling on the plasma, but the resulting equilibrium is intrinsically unstable against vertical displacements of the plasma column. To suppress this vertical instability, all shaped tokamaks require a feedback stabilization system, represented by feedback currents flowing in external coils capable of pushing the plasma back.

2.7 Heuristic model for vertical instability

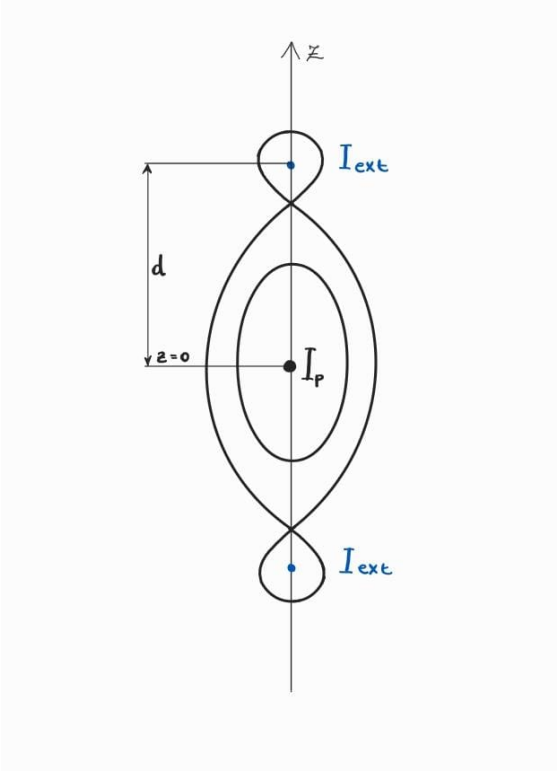

Figure 2.4: Three wires model schematic for vertical instability

To understand how the equilibrium of an elongated plasma is unstable, one can study a simple model involving currents flowing in three parallel wires - Figure

[3]DTT is the acronym for Divertor Tokamak Test. It is a tokamak device currently under construction in Frascati ENEA Research Center, Italy. Its main objective is to explore alternative solutions for the extraction of the heat generated by the fusion process.

2.4. The central wire represents the toroidal plasma current in the tokamak, it is located at z = 0 and carries a current I_p. The two other wires carry two equal currents I_{ext} and are located at $z = \pm d$, fixed in space. The central plasma wire is free to move along the z direction. A toroidal magnetic field may be added to the model, parallel to the direction of the wires, but it would play no role in this discussion. The model constructed in this way has an up-down symmetry: a double null magnetic configuration, producing two X-points, on the plane orthogonal to the wires.

In c.g.s. units, the equation of motion of the plasma wire is:

$$\mu\ddot{z} = \frac{4I_p I_{\text{ext}}}{c^2}\frac{z}{d^2 - z^2} \tag{2.20}$$

where μ is the linear mass density of the plasma wire, c is the speed of light, and the over-dot indicates derivative with respect to time.

Neglecting self and mutual induction currents, I_{ext} and I_p remain constant as the plasma wire is displaced. For $z \ll d$, the solution of equation (2.20) is

$$z = z_0 \exp^{t/\tau_{in}} \tag{2.21}$$

where

$$\tau_{in} = d\sqrt{\left(\frac{\mu c^2}{4I_p I_{\text{ext}}}\right)} = \frac{1}{2}\tau_A\sqrt{\left(\frac{I_p}{I_{\text{ext}}}\right)} \tag{2.22}$$

is an inertial time representing the instability growth time, and τ_A is the Alfvén time, based on current I_p and distance d.

One can define:

$$\gamma_H = \frac{1}{d}\sqrt{\frac{4I_P I_{ext}}{\mu c^2}} \tag{2.23}$$

In this ideal model, the instability is suppressed by the presence of a conducting wall - as the one of the vacuum chamber -, provided that this wall is not far from the plasma. Consider the case in which the X-points fall outside of the conducting shell. To allow the magnetic field produced by the external currents to penetrate across the wall and create conditions for elongated plasma equilibrium, the wall should not be a perfect conductor. However, on fast inertial time scales, wall resistivity can be neglected and the wall behaves as a perfect conductor. When the plasma is displaced from its equilibrium position, currents are induced at the wall. The sign of this currents is such that the corresponding forces oppose plasma motion. The effect is equivalent to that of two currents $\pm\delta I$ localized at the same spatial positions as the external currents.

Consider, instead of the central plasma wire, a uniform distribution of current having elliptical section with minor and major semi-axis a and b, respectively. It is possible to write:

$$\frac{I_{ext}}{I_p} \approx \frac{a-b}{a+b}\frac{d^2}{a^2+b^2} \tag{2.24}$$

which is a relation depending only on geometrical parameters of the model [18].

In the perfectly conducting limit, one can write an equation for the induced currents:

$$L\dot{\delta I} = DLI_{\text{ext}}\frac{\dot{z}}{d} \tag{2.25}$$

where L is an effective inductance and D a dimensionless proportionality constant which depends on the distance between the plasma and the wall and its geometry. We can integrate in time equation (2.25), and modify the equation of motion to include the effects of the induced currents:

$$\begin{aligned}\mu\ddot{z} &= \frac{4I_pI_{\text{ext}}}{c^2}\frac{z}{d^2-z^2} - \frac{4I_p\delta I}{c^2}\frac{d}{d^2-z^2} \\ &\approx 4\frac{I_pI_{\text{ext}}}{c^2}(1-D)\frac{z}{d^2} \quad \text{in the limit} \quad z \ll d\end{aligned} \tag{2.26}$$

For $D > 1$, the solution to this equations are stable, meaning that a displacement of the plasma current from its equilibrium position gives rise to an oscillatory motion with a characteristic frequency

$$\omega = \pm\omega_H = \sqrt{D-1}\gamma_H \tag{2.27}$$

This stability condition is usually satisfied in well-designed tokamaks.

Ref. [19] obtains the geometrical factor D analytically, for the case of confocal elliptic sections of the plasma and the wall, and uniform plasma current density distribution:

$$D = \frac{b+a}{b-a}\left(\frac{b+a}{b_w+a_w}\right)^2 \tag{2.28}$$

where a_w, b_w are minor and major axes of the wall elliptical section, respectively.

Even if we assume that this ideal stability condition, $D > 1$, is satisfied, vertical displacements may still grow in time on a time scale longer than τ_{in} if one takes into account wall resistivity.

Take equation (2.25) and add an extra term to account for the resistivity of the wall:

$$R\delta I + L\dot{\delta I} = DLI_{\text{ext}}\frac{\dot{z}}{d} \tag{2.29}$$

One can modify the equation of motion, in the limit $z \ll d$, as:

$$\mu\ddot{z} = 4\frac{I_p I_{\text{ext}}}{c^2}\frac{z}{d^2 - z^2} - 4\frac{I_p \delta I}{c^2 d} \tag{2.30}$$

The quantity $\dot{\delta I}$ can be obtained by deriving in time this equation and then using equation (2.29) to eliminate it, one finally gets:

$$\dddot{z} + \frac{1}{\tau_R}\ddot{z} + \omega_H^2 \dot{z} - \frac{1}{\tau_R}\frac{\omega_H^2}{D-1}z = 0 \tag{2.31}$$

where $\tau_R = L/R$ is the effective resistive wall penetration time.

Looking for solutions of the type $z \sim z_0 e^{(\gamma t)}$, we get a cubic dispersion relation for complex γ

$$\gamma^3 + \frac{1}{\tau_R}\gamma^2 + \omega_H^2\gamma - \frac{1}{\tau_R}\frac{\omega_H^2}{D-1} = 0 \tag{2.32}$$

In the limit $\omega_H \tau_R \gg 1$, the two oscillatory roots of this dispersion relation are damped and have complex frequency:

$$\omega = \pm\omega_H - i\frac{D}{2(D-1)\tau_R} \tag{2.33}$$

where $\gamma = -i\omega$ was set. The third root corresponds to a purely growing resistive instability with a growth rate:

$$\gamma = \frac{1}{(D-1)\tau_R} \equiv \gamma_R \tag{2.34}$$

Typically, the resistive wall time in tokamak devices is of the order of a few milliseconds.

2.8 Analytical derivation of the mode structure

The derivation of the mode structure is thoroughly explained in Refs. [20], [21] and [22].

In this contest I will report only the expressions of the quantities that will be useful for the next section for the computation of the dispersion relation. The starting equilibrium is assumed to be described by the following:

- The magnetic fiels is $\vec{B} = \hat{e}_z \times \nabla\psi + B_z\hat{e}_z$, where $\hat{e}_z$ is the unit vector along the ignorable z-direction mimicking the toroidal coordinate, B_z is a constant.

- The plasma flow is $\vec{v} = \hat{e}_z \times \nabla\phi + v_z\hat{e}_z$.
- Since toroidal effects do not play any significant role for the vertical modes, the tokamak is approximated with a straight tokamak model - a cylindrical structure with elliptic cross section. In the low-β limit, B_z and v_z fields decouple from ψ and ϕ. Therefore, the magnetic flux function, ψ, and the streamfunction, ϕ, obey the reduced ideal-MHD model, introduced in section 2.4.
- Use elliptical coordinates(μ, θ): $x = A\sinh(\mu)\cos(\theta)$, $y = A\cosh(\mu)\sin(\theta)$ with $A = \sqrt{b^2 - a^2}$. The plasma lies in the region inside an elliptical boundary μ_b with minor semi-axis a and major semi-axis b, whereas outside of this region vacuum is assumed. In the following, superscripts '-' and '+' are associated to quantities in the plasma or vacuum region, respectively.
- The current density is assumed to be uniform up to μ_b and to vanish to zero beyond that: $J_{eq}(\mu) = 2H(\mu_b - \mu)$, where $H(x)$ is the Heaviside unit step function. Similarly, the equilibrium plasma density profile is assumed to be $\rho_{eq} = H(\mu_b - \mu)$.
- In Ref. [18], it was found that the magnetic flux behaved as:

$$\psi = \psi_{eq}^{-}(x, y) = \frac{1}{2}\left(\frac{x^2}{a^2} + \frac{y^2}{b^2}\right) \quad \text{for } \mu < \mu_b \tag{2.35}$$

and

$$\psi_{eq}^{+}(\mu, \theta) = \frac{1}{2} + \frac{ab}{r_0^2}\left\{\mu - \mu_b + \frac{e_0}{2}\sinh\left[2\left(\mu - \mu_b\right)\right]\cos\left(2\theta\right)\right\} \quad \text{for } \mu > \mu_b \tag{2.36}$$

These characteristics describe an equilibrium which is easy to treat analytically.

One can now perturb the equilibrium by adding small quantities indicated by '~': $\psi(\mu, \theta, t) = \psi_{eq}(\mu, \theta) + \tilde{\psi}(\mu, \theta)e^{\gamma t}$ and $\phi(\mu, \theta, t) = \tilde{\phi}(\mu, \theta)e^{\gamma t}$ where $\gamma = -i\omega$. After this assumption the linearized version of the reduced MHD model are:

$$\gamma\tilde{\psi} + [\tilde{\phi}, \psi_{eq}] = 0 \tag{2.37}$$

$$\gamma\nabla \cdot (\rho_{eq}\nabla\tilde{\phi}) = [\tilde{\psi}, J_{eq}] + [\psi_{eq}, \tilde{J}] \tag{2.38}$$

which, when solved, give the solutions:

$$\tilde{\phi}\left(\mu, \theta\right) = \gamma\xi a\frac{\sinh\mu}{\sinh\mu_b}\cos\theta \quad \text{for } \mu < \mu_b \tag{2.39}$$

where ξ is the vertical displacement of the plasma column. And:

$$\tilde{\psi}^{-}(\mu,\theta) = -\frac{\xi}{b}\frac{\cosh\mu}{\cosh\mu_b}\sin\theta \tag{2.40}$$

$\tilde{U}, \tilde{J}, \nabla\rho_{eq}, \nabla J_{eq}$ vanish inside the elliptical boundary. In the presence of a wall, the solution of the magnetic flux for $\mu > \mu_b$:

$$\tilde{\psi}^{+}(\mu,\theta) = -\frac{\xi_\infty}{b}\exp\left[-(\mu-\mu_b)\right]\sin\theta + \frac{\xi_{ext}}{b}\frac{\cosh\mu}{\cosh\mu_b}\sin\theta \tag{2.41}$$

where ξ_∞ is the amplitude of the rigid vertical displacement in the limit where the wall is moved to infinity, and the term proportional to ξ_{ext} represents the contribution due to the image currents that form on the wall when it is at finite distance. Continuity of the flux at the plasma boundary imposes that $\xi = \xi_\infty - \xi_{ext}$ - the actual displacement is reduced when a wall is present. A perturbed current sheet forms at the plasma boundary:

$$\tilde{J}(\mu,\theta) = \tilde{j}_b(\theta)\,\delta(\mu-\mu_b) = \frac{1}{h^2}\left(\frac{\partial\tilde{\psi}^{+}}{\partial\mu} - \frac{\partial\tilde{\psi}^{-}}{\partial\mu}\right)\Bigg|_{\mu_b}\delta(\mu-\mu_b) \tag{2.42}$$

where $\delta(x)$ is the Dirac delta function and

$$\tilde{j}_b(\theta) = \frac{2(a+b)}{b^2(a^2+b^2)}\frac{\xi_\infty\sin\theta}{1+e_0\cos(2\theta)} \tag{2.43}$$

2.9 Dispersion relation

One can now derive analytically the dispersion relation for $n = 0$, vertical modes.

Denote by Ω the volume occupied by the plasma up to $\mu = \mu_b + \epsilon$, which includes the perturbed current sheet at the plasma boundary.

Introduce the auxiliary streamfunction $\tilde{\phi}^{\dagger}$ equal to the complex conjugate streamfunction inside Ω and vanishing in the vacuum region. By multiplying the equation of motion 2.38 by $\tilde{\phi}^{\dagger}/2\gamma^{*}$, and integrating over the whole volume extending to infinity, we obtain:

$$-\gamma^2\frac{1}{2}\int_\Omega d^3x\rho_{eq}\vec{\xi}\cdot\vec{\xi}^{*} = -\frac{1}{2}\int_\Omega d^3x\vec{\xi}^{*}\cdot[(\tilde{\vec{J}}\times\vec{B}_{eq}) + (\vec{J}_{eq}\times\tilde{\vec{B}})] \tag{2.44}$$

where $\vec{\xi} = \hat{e}_z\times\nabla\tilde{\phi}/\gamma$.

Thanks to work of, for instance, [23], the dispersion relation can be found as

$$-\gamma^2 = \frac{\delta W}{\delta I} \tag{2.45}$$

with

$$\delta I = \frac{1}{2}\int_\Omega \rho_{eq}\vec{\xi}\cdot\vec{\xi}^* d^3x \tag{2.46}$$

and

$$\delta W = -\frac{1}{2}\int_\Omega \vec{\xi}^*\cdot F(\vec{\xi}) d^3x \tag{2.47}$$

where $\vec{F}(\xi) = [(\tilde{\vec{J}}\times\vec{B}_{eq}) + (\vec{J}_{eq}\times\tilde{\vec{B}})]$ is the force density operator in the limit where β effects are negligibly small.

In the potential energy integral, δW, wall effects are included through the perturbed magnetic flux. δW is a real quantity, independent of the mode frequency in the limit of an ideal wall, but frequency dependent when the wall is resistive.

Since we are using elliptical coordinates, $d^3x = h^2 d\theta d\mu dz$. The scale factor h originates from the normalization and its square amounts to $h^2 = A^2\left(\cosh(2\mu)+\cos(2\theta)\right)/2$. Then:

$$\delta I = \frac{1}{2}\int_\Omega d^3x\rho_{eq}\frac{\nabla\tilde{\phi}\cdot\nabla\tilde{\phi}^*}{|\gamma|^2} = \frac{\pi}{2}abL_z\xi^2 \tag{2.48}$$

where L_z is the length of the straight tokamak, and ξ is real and represents the amplitude of the vertical displacement. The perturbed energy integral is

$$\delta W = \frac{1}{2}\int_\Omega d^3x\left(\vec{e}_z\times\frac{\nabla\tilde{\phi}^*}{\gamma^*}\right)\cdot\left(\tilde{J}\nabla\psi_{eq} + J_{eq}\nabla\tilde{\psi}\right) \tag{2.49}$$

which can be further manipulated:

$$\begin{aligned} 1^{st}\text{ term:}\quad \frac{1}{2}\int_\Omega d^3x\tilde{J}\nabla\psi_{eq}\left(\vec{e}_z\times\frac{\nabla\tilde{\phi}^*}{\gamma^*}\right) &= \frac{L_z}{2}\int_0^{2\pi}d\theta\int_0^{\mu_b+\epsilon}d\mu h^2\tilde{j}_b(\theta)\times \\ &\quad\times\delta(\mu-\mu_b)\nabla\psi_{eq}\cdot\left(\vec{e}_z\times\frac{\nabla\tilde{\phi}^\dagger}{\gamma^*}\right) \\ &= \frac{\pi}{2}\frac{a+b}{b^3}L_z\xi_\infty\xi \end{aligned} \tag{2.50}$$

$$\begin{aligned} 2^{nd}\text{ term:}\quad \frac{1}{2}\int_\Omega d^3xJ_{eq}\nabla\tilde{\psi}\left(\vec{e}_z\times\frac{\nabla\tilde{\phi}^*}{\gamma^*}\right) &= \frac{L_z}{2}\int_0^{2\pi}d\theta\int_0^{\mu_b+\epsilon}d\mu h^2 J_{eq}\times \\ &\quad\times\nabla\tilde{\psi}^-\cdot\left(\vec{e}_z\times\frac{\nabla\tilde{\phi}^\dagger}{\gamma^*}\right) \\ &= -\frac{\pi}{2}\frac{a^2+b^2}{ab^3}L_z\xi^2 \end{aligned} \tag{2.51}$$

where the relation $(a^2+b^2)/(2a^2b^2) = 1$, coming from the normalization choice, was used.

We can introduce the quantity

$$D_w = \frac{\xi_{ext}}{\hat{e}_0 \xi_\infty} \tag{2.52}$$

where $\hat{e}_0 = (e_0 b)/(a+b)$. Combining all of the previous result:

$$\delta W = -\frac{\pi}{2} L_z \frac{1 - a/b}{ab} \frac{1 - D_w}{1 - \hat{e}_0 D_w} \xi^2 \tag{2.53}$$

and, finally:

$$\gamma^2 = \frac{1 - a/b}{a^2 b^2} \frac{1 - D_w}{1 - \hat{e}_0 D_w} \tag{2.54}$$

In this dispersion relation, all wall effects are included through the function D_w.

Notice that parameters a and b were normalized to the scale length $r_0 = ab/\left[(a^2+b^2)/2\right]^{1/2}$. When reintroducing dimensions, the expression of the dispersion relation becomes:

$$(\gamma \tau_A)^2 = \frac{r_0^4}{a^2 b^2} \left(1 - \frac{a}{b}\right) \frac{1 - D_w}{1 - \hat{e}_0 D_w} \tag{2.55}$$

One can state that the dispersion relation for n = 0 vertical modes depends on geometrical parameters a and b, and on D_w, which is determined by the geometry and the resistivity of the wall. In the case of a perfectly conducting wall, D_w is a real quantity, independent of γ, that can be reduced to the parameter D introduced in section 2.7. In this case, D_w determines the mode stability, since the sign of γ^2 depends on the sign of $(1 - D_w)$. In the case of a resistive wall, D_w is a function of γ, resulting in a dispersion relation that is cubic in this variable. The next sections contain additional details on these different scenarios.

2.9.1 No-wall limit

The no wall limit is equivalent to a scenario in which the wall is moved to infinity, resulting in $\xi_{ext} = 0$. Consequently, $D_w = 0$ and γ^2 becomes a positive real value for $b > a$ or vanishes in the circular limit $b = a$. The mode growth rate is

$$\gamma = \frac{r_0^2}{ab} \left(1 - \frac{a}{b}\right)^{\frac{1}{2}} \tau_A^{-1} \equiv \gamma_\infty \tag{2.56}$$

In the limit of small ellipticity, this is equivalent to the definition 2.23.

2.9.2 Ideal wall case

Assume now to represent the wall with an elliptical coordinate surface μ_w, confocal to the elliptical plasma boundary μ_b, $\mu_w \geq \mu_b$. If this wall is ideal, the perturbed magnetic flux must vanish on μ_w. It follows that

$$\frac{\xi_{ext}}{\xi_\infty} = \frac{\exp(-(\mu_w - \mu_b))\cosh(\mu_b)}{\cosh(\mu_w)} = \frac{1+\exp(2\mu_b)}{1+\exp(2\mu_w)} \tag{2.57}$$

and thus, after some algebra, using the definition 2.52:

$$D_w = \frac{b^2+a^2}{(b-a)^2}\frac{b_w - a_w}{b_w} \equiv D \tag{2.58}$$

If $D > 1$, γ^2 is negative and the vertical mode oscillates with a real frequency:

$$\omega = \pm\omega_0 = \pm\left[\frac{D-1}{1-\hat{e}_0 D}\right]^{\frac{1}{2}}\gamma_\infty \tag{2.59}$$

which reduces to ω_H, in agreement with the heuristic model, in the limit of small ellipticity.

The only solutions of the dispersion relation in this case are the VDOM solutions, meaning that the ideal wall provides a passive feedback stabilization on the vertical instability.

The singularity in the domain of ω happens for the maximum possible value of D when $\mu_w = \mu_b$: the oscillation frequency goes to infinity, but the amplitude of the displacement ξ vanishes.

As D decreases, the oscillatory solution is found.

The marginally stable value $D = 1$ is obtained when $\mu_w = 2\mu_b$, corresponding to the wall intercepting the X-points.

Values of $D < 1$ for which it is not possible to have a passive feedback are found when the X-points lie inside the volume bound by the wall.

2.9.3 Resistive wall case

The last case is the most realistic one: a resistive wall.

The perturbed magnetic flux is not zero on the wall in this case, but can diffuse on the resistive wall time scale. There is a need to identify three different regions:

- $\mu \leq \mu_b$: inside the plasma, the perturbed flux $\tilde{\psi} = \tilde{\psi}^-(\mu,\theta) = -\frac{\xi}{b}\frac{\cosh\mu}{\cosh\mu_b}\sin\theta$

- $\mu_b \leq \mu \leq \mu_w$: in the vacuum region between the plasma and the wall, $\tilde{\psi} = \tilde{\psi}^+(\mu,\theta) = -\frac{\xi_\infty}{b}\cosh[-(\mu-\mu_b)]\sin\theta + \frac{\xi_{ext}}{b}\frac{\cosh\mu}{\cosh\mu_b}\sin\theta$;
- $\mu > \mu_w$: outside the wall, $\tilde{\psi} = \tilde{\psi}_{out}$, solution of $\nabla^2\tilde{\psi}_{out} = 0$ and decaying to zero at infinity.

The relevant solution is $\tilde{\psi}_{out}(\mu,\theta) = \psi_0\cosh(-(\mu-\mu_w))\sin\theta \quad \text{for } \mu \geq \mu_w + \delta_w$, where δ_w is a small parameter representing the average width of the wall.

Two conditions determine ψ_0 and D_w:

- continuity of the flux at the wall: $\tilde{\psi}^+(\mu_w,\theta) = \tilde{\psi}_{out}(\mu_w,\theta)$, from which we get:

$$\psi_0 = -\frac{\xi_\infty}{b}\cosh(-(\mu_w-\mu_b)) + \frac{\xi_{ext}}{b}\frac{\cosh\mu_w}{\cosh\mu_b} \tag{2.60}$$

- consider the resistive Ohm's law for the perturbed magnetic flux within the wall. After proper normalization:

$$\nabla^2\tilde{\psi}_w = \frac{\gamma}{\varepsilon_\eta}\tilde{\psi}_w \tag{2.61}$$

  where $\varepsilon_\eta = (\eta\tau_A c^2)/(4\pi r_0^2)$ is the inverse of the relevant dimensionless Lundquist number, and η is the wall resistivity. On the right-hand side of the equation we can neglect the dependence on μ of the perturbed flux because of the thinness of the wall. Set $\tilde{\psi} = \hat{\psi}(\mu)\sin\theta$ and assume the ordering $\partial_\mu^2\hat{\psi} \sim \hat{\psi}/\mu_w\delta_w \gg \hat{\psi}$. We can then approximate equation 2.61 as

$$\frac{d^2\hat{\psi}}{d\mu^2} = h^2\frac{\gamma}{\varepsilon_\eta}\psi_0 \tag{2.62}$$

  and, integrating across the thin wall:

$$\int_{\mu_w}^{\mu_w+\delta_w}\frac{d^2\hat{\psi}}{d\mu^2}d\mu = \int_{\mu_w}^{\mu_w+\delta_w} h^2\frac{\gamma}{\varepsilon_\eta}\psi_0 d\mu \tag{2.63}$$

  Previously defined h strictly speaking depends on both μ and θ; however, in the small wall ellipticity, the θ modulation of h along the wall is small and thus $h(\mu_w,\theta) \approx b_w$. Carrying out the integration, we find:

$$\left(\frac{d\hat{\psi}_{out}}{d\mu} - \frac{d\hat{\psi}^+}{d\mu}\right)\Bigg|_{\mu_w} = \frac{\gamma\delta_w b_w^2}{\varepsilon_\eta}\psi_0 \tag{2.64}$$

  which is equivalent to:

$$-\frac{\xi_\infty}{b}\exp(-(\mu_w-\mu_b)) - \frac{\xi_{ext}}{b}\frac{\sinh\mu_w}{\cosh\mu_b} = \left(1 + \frac{\gamma\delta_w b_w^2}{\varepsilon_\eta}\right)\psi_0 \tag{2.65}$$

These results can be used to find:

$$D_w(\gamma) = D\frac{\gamma\tau_\eta}{1+\gamma\tau_\eta} \tag{2.66}$$

and

$$\psi_0 = -\frac{\xi_\infty}{b}\frac{b_w}{a+b}\frac{e_0 D}{1+\gamma\tau_\eta} \tag{2.67}$$

where the definition of D is 2.58 and

$$\tau_\eta = \frac{b_w^3}{a_w+b_w}\frac{\delta_w}{\varepsilon_\eta} \tag{2.68}$$

is the resistive wall time, normalized to the relevant Alfvén time.

The stability parameter D_w is now a function of γ due to the finite wall resistivity.

In the ideal wall limit, $\tau_\eta \to \infty$ and thus $D_w(\gamma) \to D$.

Substituting $D_w(\gamma)$ into equation 2.55, we get the dispersion relation for vertical displacements in the case of feedback stabilization via a resistive wall:

$$\gamma^3 + \gamma^2\frac{1}{\tau_\eta}\frac{1}{1-\hat{e}_0 D} + \gamma\omega_0^2 + \omega_0^2\frac{1}{\tau_\eta}\frac{1}{1-D} = 0 \tag{2.69}$$

with ω_0 is defined in 2.59.

Equation 2.69 is in agreement with the dispersion relation obtained from the heuristic model.

In the realistic limit of $\omega_0\tau_\eta \gg 1$, one can determine the three roots of the dispersion relation. For $D > 1$, there are two damped oscillatory roots and an unstable growing solution:

$$\omega = \pm\omega_0 - i\frac{1}{2\tau_\eta}\frac{D(1-\hat{e}_0)}{(D-1)(1-\hat{e}_0 D)} \tag{2.70}$$

These two oscillatory, weakly damped roots of equation correspond to the two VDOM and oscillate at a frequency slightly below the poloidal Alfvén frequency. The resistive wall introduces a small damping rate of the order of the inverse resistive wall time. Moreover, the third root, corresponding to an unstable mode, growing on the resistive wall time scale:

$$\gamma = \frac{1}{(D-1)\tau_\eta} \tag{2.71}$$

This unstable mode is normally suppressed by means of active feedback control systems.

2.9.4 $\omega^2\tau_A^2$

Consider the dispersion relation 2.69, which we rewrite as:

$$\gamma^3 + \frac{\gamma^2}{\tau_\eta}\frac{1}{1-\hat{e}_0 D} + \gamma\gamma_\infty^2\frac{D-1}{1-\hat{e}_0 D} - \frac{\gamma_\infty^2}{\tau_\eta}\frac{1}{1-\hat{e}_0 D} = 0 \tag{2.72}$$

Also γ_∞ and D can be recast in equivalent forms, which make explicit their dependence on the parameters $\kappa = b/a$ - elongation - and b/b_w, which represents the distance between the wall and the plasma:

$$\gamma_\infty = \frac{2\kappa}{\kappa^2+1}\left(\frac{\kappa-1}{\kappa}\right)^{\frac{1}{2}}\tau_A^{-1} \tag{2.73}$$

and

$$D\left(\kappa, \frac{b}{b_w}\right) = \frac{\kappa^2+1}{(\kappa-1)^2}\left\{1 - \left[1 - \frac{\kappa^2-1}{\kappa^2}\left(\frac{b}{b_w}\right)^2\right]^{\frac{1}{2}}\right\} \tag{2.74}$$

Figure 2.5 and 2.6 show the behaviour of the quantity $\omega^2\tau_A^2$ as a function of the parameter b/b_w and of the elongation κ, respectively.

These will be used in chapter 4.

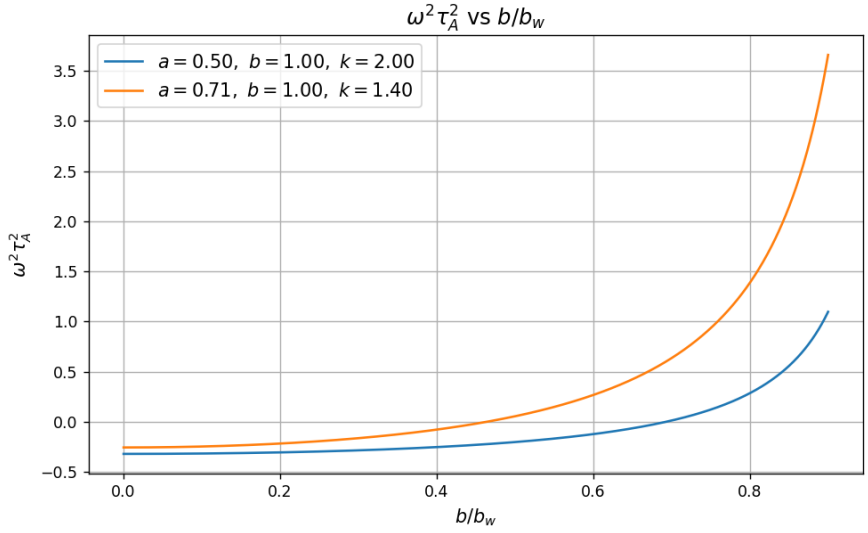

Figure 2.5: $\omega^2\tau_A^2$ as a function of the parameter b/b_w: in blue, the case $\kappa = 2.0$; in orange, the case of $\kappa = 1.4$.

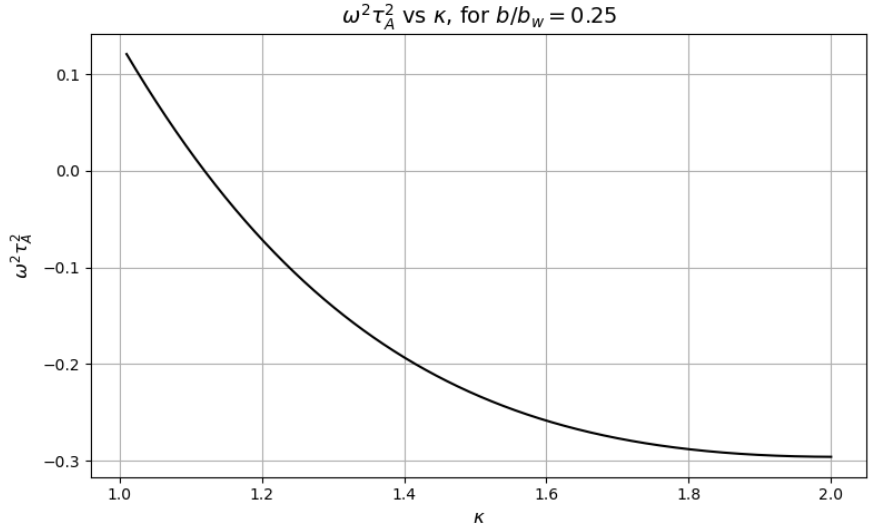

Figure 2.6: $\omega^2\tau_A^2$ as a function of the parameter κ for fixed $b/b_w = 0.25$.

Chapter 3

NIMROD MHD model

3.1 Overview of the NIMROD code

Numerical simulations are exceptionally important to the advancement of magnetically confined fusion. Numerical modeling in this field is challenging. First and foremost, the fluid model of magnetized plasmas forms a system of equations that is stiff and very anisotropic. Furthermore, when applied to the modeling of plasma fusion experiments, these equations need to be solved in realistic geometric configurations in order to capture the global nature of the activity.

To be able to address these issues, and to study these phenomena with realistic dynamics, the NIMROD project was born [24]. The NIMROD acronym stands for Non-Ideal Magnetohydrodynamics with Rotation, Open Discussion, and the project itself aims at developing a code that is able to address multiple issues arising in present day fusion experiments, especially concerning various forms of nonlinear global magnetic activity.

NIMROD is a very complex code, and going into the details of the methods it uses to evolve the equations and compute the quantities characterizing the system would take much space. To give a general idea, NIMROD uses the semi-implicit finite difference method to evolve time, and the finite element method to take care of the spatial dimensions.

For further details on the project, we refer to the web-page of the NIMROD team [25] and to the numerous scientific papers which discuss the topic.

3.2 Pitagora supercomputer

The amount of workload that needs to be handled in order to perform this type of numerical simulations would be heavy on any common computer. For this reason, there is the need for more powerful systems. Specifically for the numerical simulations presented in this thesis, the supercomputer Pitagora was used.

Pitagora is a new supercomputer hosted by CINECA - Consorzio Interuniversitario del Nord-Est per il Calcolo Automatico - and currently built in CINECA's headquarter in Casalecchio di Reno, Bologna, Italy. It is fully dedicated to the EUROFusion community to conduct research on nuclear fusion.

The cluster is supplied by Lenovo corp. and is composed of two partitions: a general purpose partition cpu-based named DCPG (Data Centric and General Purpose) and an accelerated partition based on NVIDIA H100 accelerators named Booster [26]. Figure 3.1 shows an overview of the system architecture of Pitagora.

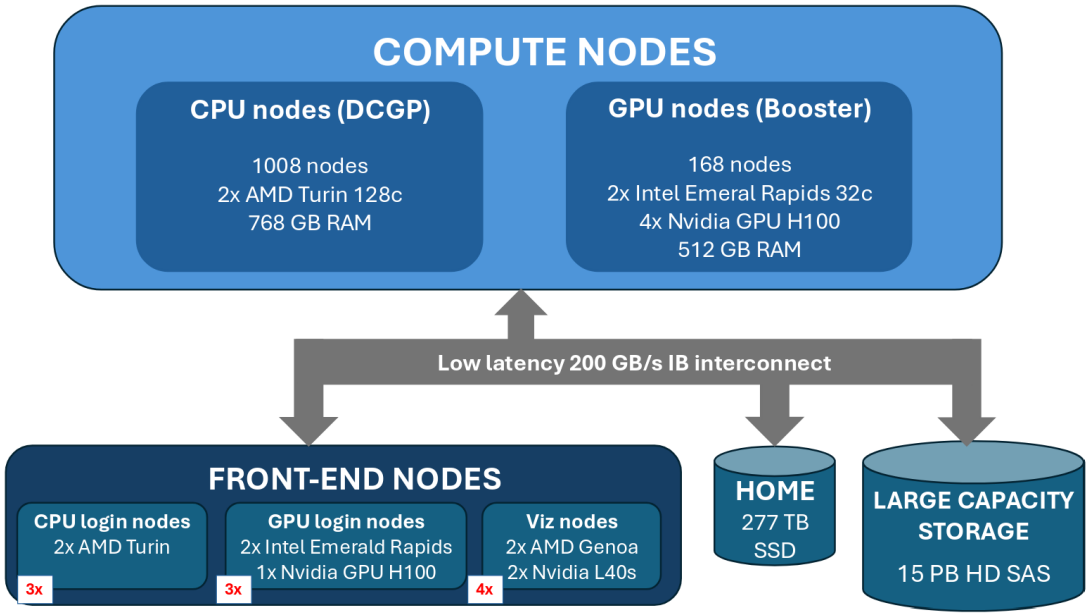

Figure 3.1: System architecture of Pitagora Supercomputer [26]

3.3 Simulation set-up

The work of this thesis makes use of simulations performed in NIMROD. For this reason this section is dedicated to providing details on the simulation set-up.

3.3.1 Linear MHD simulation model

When linear simulations are mentioned, we are referring to simulations that solve the linearized version of the single fluid resistive MHD model. This is made of the following equations:

- continuity equation:

$$\frac{\partial n}{\partial t} + \nabla \cdot (n\vec{v}) = \nabla \cdot \mathcal{D}\nabla n \tag{3.1}$$

- momentum equation:

$$mn\left(\frac{\partial}{\partial t} + \vec{v}\cdot\nabla\right)\vec{v} = \frac{1}{\mu_0}\left(\nabla\times\vec{B}\right)\times\vec{B} - \nabla p + \nabla\cdot\nu\rho\nabla\vec{v} \tag{3.2}$$

- temperature equation:

$$\frac{3}{2}\left(\frac{\partial}{\partial t} + \vec{v}\cdot\nabla\right)T = -nT\nabla\cdot\vec{v} \tag{3.3}$$

- modified Faraday's equation:

$$\frac{\partial\vec{B}}{\partial t} = -\nabla\times\left[\eta_e\left(\nabla\times\vec{B}\right) - \vec{v}\times\vec{B}\right] + \kappa_{divb}\nabla\nabla\cdot\vec{B} \tag{3.4}$$

where n and m are respectively particle density and ion mass. The total pressure of electrons and ions is p, $\vec{v}$ is the center-of-mass plasma velocity, T is the single fluid temperature. Explicit diffusive terms are included: the density diffusivity $\mathcal{D}$, the kinetic viscosity ν, the electrical diffusivity coefficient η_e, and κ_{divb}, a diffusivity coefficient used to control the $\nabla\cdot\vec{B}$ error in the induction equation.

As the simulation proceeds, NIMROD advances in time only the perturbed $n = 0$ components, while the equilibrium configuration is preserved. For nonlinear simulations, this is not always true and consequences will be discussed in the next chapter.

3.3.2 Plasma equilibrium

For simplicity of implementation in the code, the straight tokamak approximation is used, and only a single toroidal $n = 0$ mode in the axisymmetric z-direction is simulated. The simulation domain is represented by a Cartesian rectangular domain on the poloidal plane.

To reproduce the analytical equilibrium in NIMROD, we make use of the force balance relation in a linear plasma column, which in the flux coordinate ψ is:

$$\frac{d}{dt}\left[\frac{B_z^2}{2\mu_0} + p(\psi)\right] = -J_z(\psi) = -J_0 \tag{3.5}$$

B_z is the uniform and constant axial magnetic field. The analytical Heaviside function of the plasma current density is implemented in NIMROD and the value of the total current for most simulations, unless otherwise stated, is $I = 10^5$ A. The pressure profile is a linear function of the flux $p(\psi) = p_0(1 - \psi/\psi_b)$, where ψ_b is the plasma boundary. Plasma density is constant at $n_0 = 10^{19}\,\mathrm{m}^{-3}$ inside the plasma elliptical boundary, but not vanishing outside of it. NIMROD does not support vacuum, meaning that this region, which is empty in the analytical model, is filled by a cold *halo* plasma with density $n_{halo} = 10^{17}\,\mathrm{m}^{-3}$. To avoid using sharp gradients, which might generate numerical problems, the transition between the two values follows a hyperbolic tangent function:

$$n(\psi) = n_{halo} + (n_0 - n_{halo})\,\frac{[1 - \tanh(\sigma(\psi - \psi_b)/\psi_b)]}{2} \tag{3.6}$$

where parameter σ controls the width of the transition. The *halo* plasma also has a higher resistivity with respect to the hot plasma region.

3.3.3 Choice of initial perturbation

NIMROD is an initial value code, and it is important to choose the initial perturbation to which we subject the system in such a way that the it excites the right mode. The VDOM is characterized by mode numbers $n = 0$ and $m = 1$. This structure corresponds to a rigid vertical shift of the plasma column, where the term *rigid* refers to the property that the vertical flow radial profile has a nearly constant amplitude from the magnetic axis to the plasma edge. The initial perturbation that is most appropriate is a *vertical rigid shift*, or *vertical push*. This perturbation is set initially as perturbation in the magnetic field, which then perturbs the velocity according to:

$$\tilde{V} = \frac{\tilde{B}}{\mu_0 n_0 m} \tag{3.7}$$

The careful choice of initial perturbation is necessary, because VDOMs are stable modes, and therefore different initial conditions lead to a mix of different oscillatory modes. Resulting interference would cause a rapid decay of all modes, including the VDOM. This kind of consideration is the reason why it becomes convenient to introduce a forcing term in the equations of the linearized model to isolate the mode. This method will also be discussed in the next chapter.

3.3.4 Walls and simulation domain

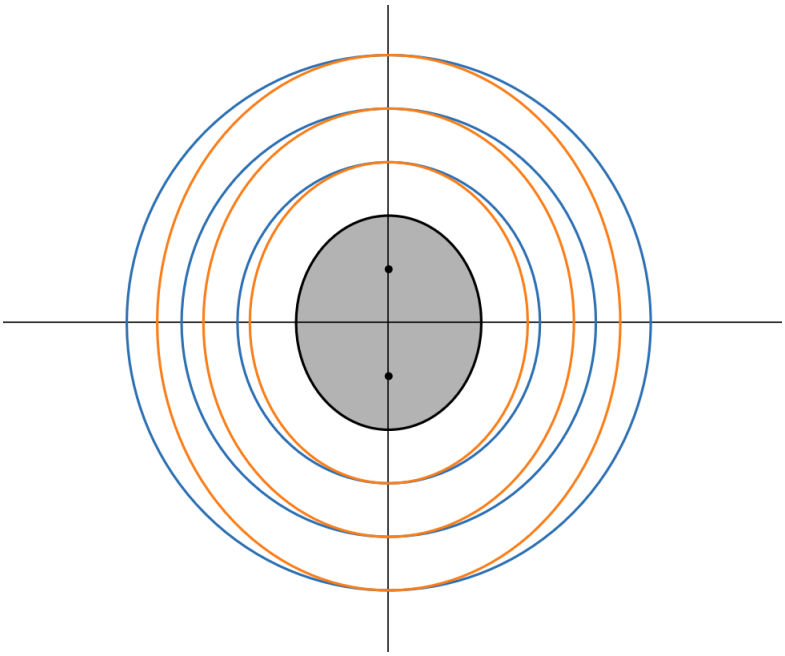

Figure 3.2: Confocal (blue) and self-similar (orange) elliptical boundaries. Plasma section is represented by the black-shaded area.

From the analytical point of view, we remind that parameters a and b represent the minor and major semi-axes of the ellipse that describes the plasma boundar; parameters a_w and b_w describe the dimensions of the elliptical wall of the vessel in which the plama is confined. They correspond to the minor and major semi-axes of the wall, respectively.

Two characteristics can vary:

- value of b/b_w, which measures the distance of the wall from the plasma elliptical boundary;
- a construction criterion:
  - confocality condition: $b_w^2 - a_w^2 = b^2 - a^2$. According to this relation, the wall dimensions generate an ellipse that has the same foci as the plasma one.
  - self-similarity condition: $b/a = b_w/a_w$. The ellipse built by using this relation has the same elongation κ as the plasma one, but different foci.

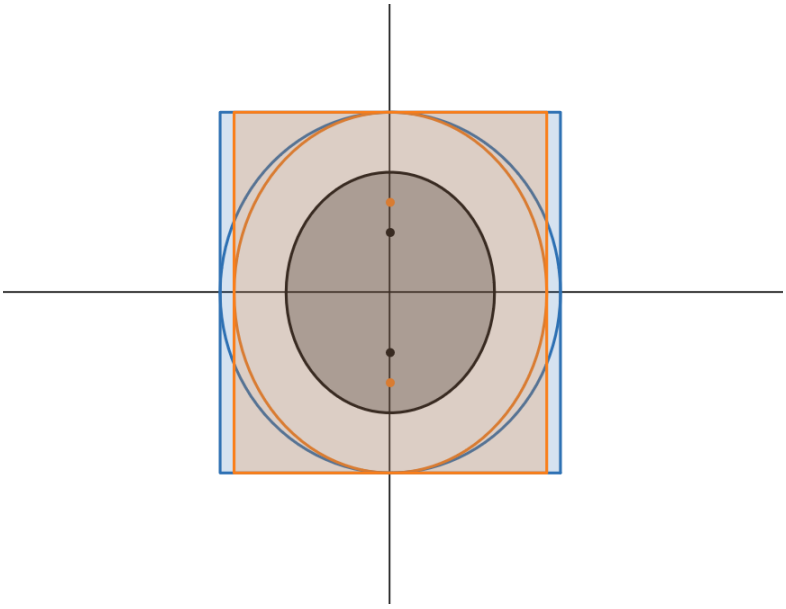

Figure 3.3: Confocal (blue) and self-similar (orange) elliptical boundaries. The black ellipse and the gray-shaded area represents the plasma boundary and section, respectively. the blue ellipse is confocal to the black one, and has the same black foci; the blue-shaded rectangle represents the corresponding simulation domain. The orange ellipse is self-similar to the black one, and its foci are shown as orange dots; the orange-shaded rectangle is the corresponding simulation domain.

Examples of walls that can be built by tuning these parameters can be seen in Figure 3.2.

As previously mentioned, the NIMROD code does not support an elliptical wall boundary and implements in its stead a rectangular one. The wall in the simulation also represents the limits of the simulating domain, and is a rectangle with height $2b_w$ and width $2a_w$. Such rectangle circumscribes the analytical ellipse with semi-axes b_w and a_w, implying that for equal values of b/b_w the simulation domain is larger than the analytical one. Figure 3.3 provides a visual depiction.

Chapter 4

Linear and nonlinear numerical results

In this chapter, results of the MHD numerical simulations performed for this thesis can be found.

Linear numerical simulations were carried out with the intention of verifying the analytical results obtained in the context of the ideal MHD model. Taking the equilibrium configuration as described in the previous chapter, we perturb it and observe the evolution. Most of the simulations are organized in *scans*, namely sets of simulations exploring different values of the geometrical parameters.

Evaluation of the nonlinear terms of the ideal MHD model is needed to further explore the behaviour of the VDOMs in a more realistic context. After applying the same type of initial perturbations as for the linear cases, temporal and spatial evolution of the system is observed in search of nonlinear phenomena.

4.1 Linear simulations

According to the theoretical analysis in Chapter 2, when the geometrical parameter $D > 1$, the solution of the dispersion relation for the axisymmetric modes yields two oscillatory damped roots. This is a stable scenario. The condition $D > 1$ represents a magnetic configuration that has the X-points outside the walls of the vessel, as depicted in Figure 4.1a.

Figure 4.1b, instead, represent the opposite case of a configuration with magnetic X-points lying inside the walls. This situation, described by $D < 1$, gives rise to an

unstable solution.

The case $D = 1$ is referred to as marginal stability, that is when the X-points intercept the wall boundary.

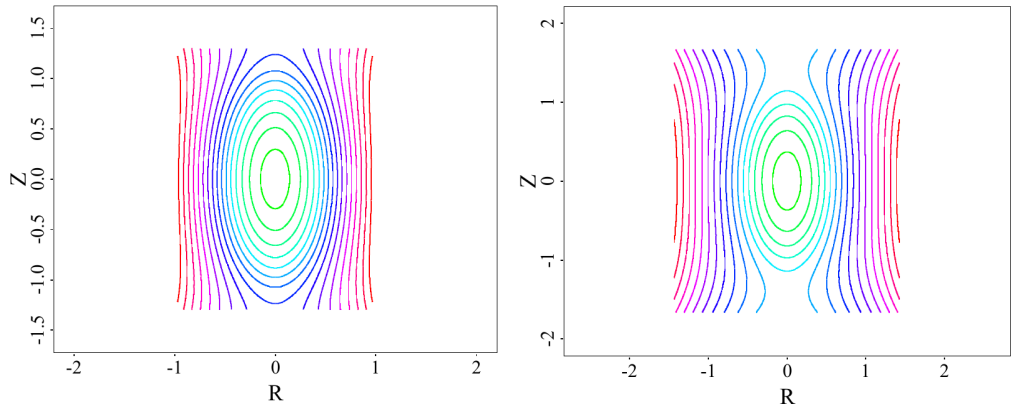

(a) Stable configuration with magnetic X-points outside the walls - $D > 1$

(b) Unstable configuration with magnetic X-points inside the walls - $D < 1$

Figure 4.1: Magnetic flux function ψ for stable and unstable configurations

4.1.1 Stable case analysis

The relevant quantity for studying vertical instabilities is the vertical component of the velocity, V_z. The plot in Figure 4.2 is chosen as an example of the type of behaviour produced by a simulations of a stable case.

In particular, Figure 4.2 represents an interval of ~ 5 ms, during which one can observe an oscillation with amplitude decreasing as time progresses. Among the frequencies of this oscillation, there is the VDOM frequency, which is estimated in this case at 12.0 kHz. We are able to measure the frequency of the VDOM in the central part of the simulation: a good time range would be from 0.5 ms to 2 ms. In this way any additional frequency which may arise from the initial transient or from the asymptotic behaviour at larger time values is neglected.

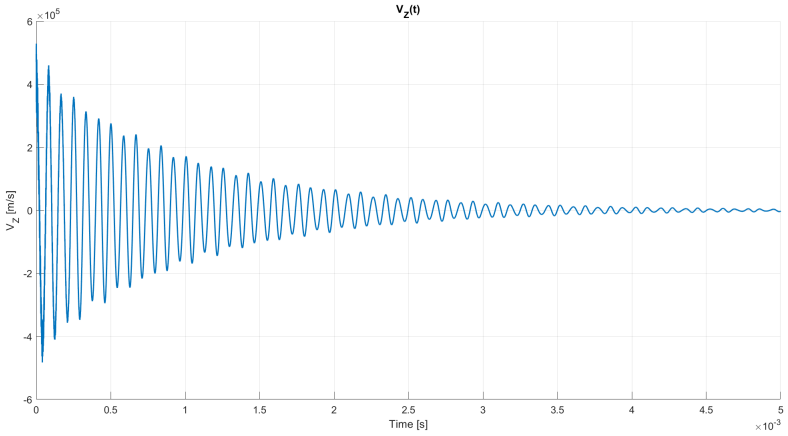

Figure 4.2: $V_z(t)$ for the case of confocal walls, $\kappa = 2.0$, $b/b_w = 0.80$

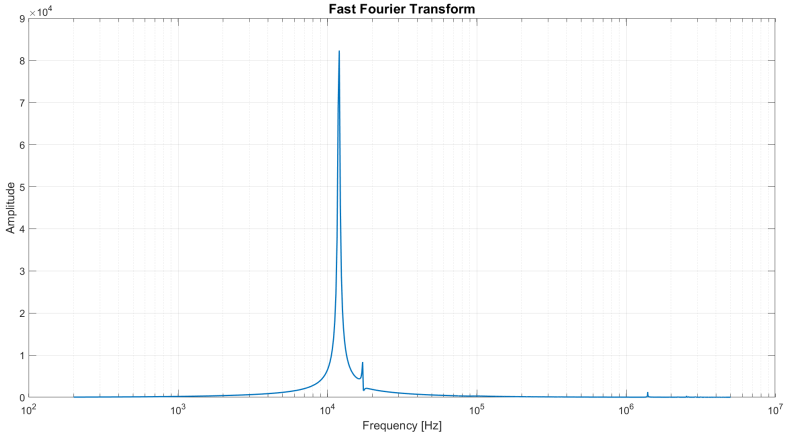

Figure 4.3: Fast Fourier Transform of the V_z data for the case confocal, $\kappa = 2.0, b/b_w = 0.8$

To evaluate the frequencies of oscillation, computational help is needed: specific sections of the data set for the vertical component of the velocity are used to compute the Fast Fourier Transform (FFT) spectrum. For this example, results are plotted in Figure 4.3. We can observe the following peaks in the spectrum:

- the highest peak corresponds to the VDOM frequency;
- one smaller peak is found at a frequency $\sim$ 16.7 kHz, and is still under investigation;
- additional smaller peaks can be found at higher frequencies - in the order of MHz. These are due to numerical instabilities of the simulations, do not

represent any physical oscillation and can thus be safely ignored.

The abscissa of the FFT peaks represent the real frequencies of oscillation of the plasma in the simulation. Since the value of $\omega^2\tau_A^2$ is of interest to us, we proceed to compute these two quantities:

- values of ω are easily obtained according to the relation $\omega = 2\pi f$, where f is the VDOM frequency in Hz as read on the FFT spectrum;
- values of the Alfvén time can be computed starting from the parameters of the simulation and according to:

$$\tau_A = 2\pi \frac{ab}{I_p}\sqrt{\frac{\rho_m}{\mu_0}} \tag{4.1}$$

  where $I_p = 10^5 A$ is the plasma current, $\rho_m = nm_{\text{deut}}$ is the mass density, n is the particle density and m_{deut} is the deuteron mass, and μ_0 is the magnetic vacuum permeability.

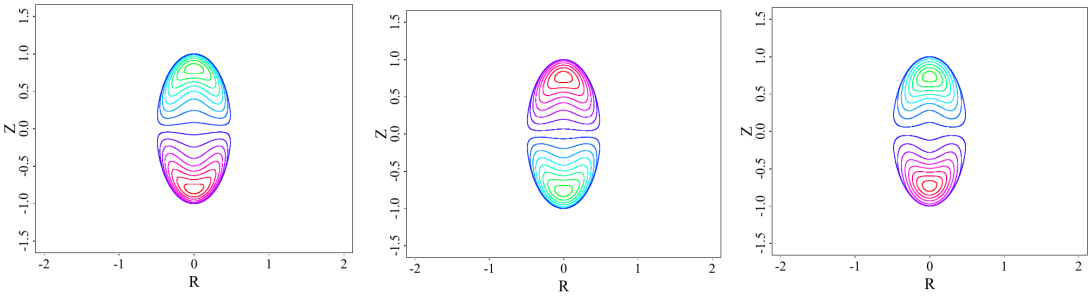

(a) $t = 5{\times}10^{-5}$ µs **(b)** $t = 1{\times}10^{-4}$ µs **(c)** $t = 1.5{\times}10^{-4}$ µs

Figure 4.4: Linear simulation of confocal walls, $\kappa = 2.0$, $b/b_w = 0.8$: contour plots of $\tilde{p}$

Figure 4.4 shows the contour plots of $\tilde{p}$, perturbed pressure field, and more specifically a time range in which one can see an entire period of oscillation.

4.1.2 Growing case analysis

Figure 4.5 shows the behaviour of V_z when the oscillation is unstable. The quantity grows exponentially, and is characterized by a growth rate γ. It is possible to use the relation:

$$\omega = -i\gamma \tag{4.2}$$

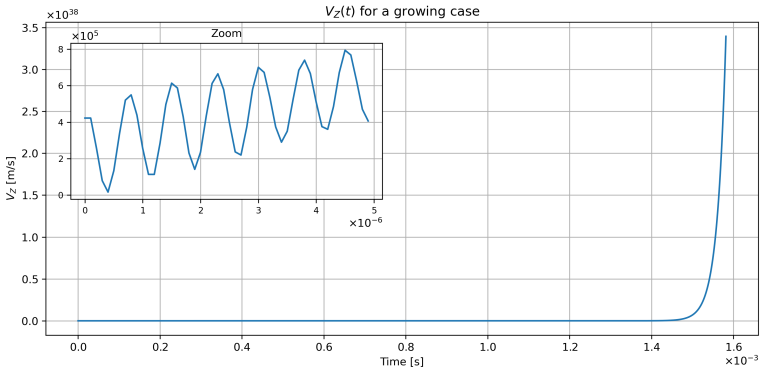

Figure 4.5: $V_z(t)$ of confocal $\kappa = 1.4, b/b_w = 0.4$

The asymptotic value of the growth rate for this example is $\gamma = 4.76 \times 10^5$.

Other quantities show the same behaviour: Figure 4.6 shows the growth of the magnetic energy in logarithmic scale.

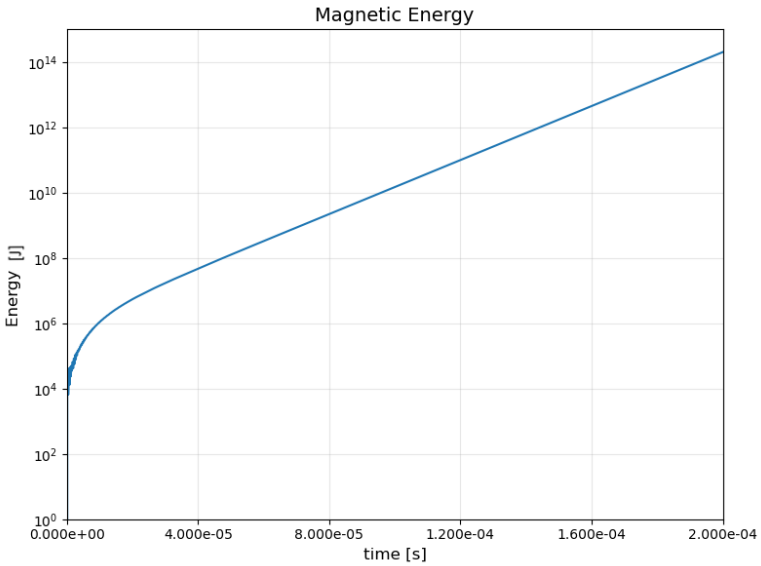

Figure 4.6: Logarithm of the magnetic energy for the confocal walls, $\kappa = 1.4, b/b_w = 0.4$

4.1.3 Confocal wall scans

The first sets of simulations were performed once for $\kappa = 2.0$ and once for $\kappa = 1.4$.

Used data appears in table 4.1.

Table 4.1: Data for confocal wall scans

Confocal walls, $\kappa = 1.4$				
$\tau_A = 7.318\mu s$				
a [m]	b [m]	a_w [m]	b_w [m]	b/b_w
0.714	1.00	2.40	2.50	0.4
		1.87	2.00	0.5
		1.38	1.67	0.6
		1.25	1.43	0.7
		1.04	1.25	0.8
		0.974	1.20	0.83
Confocal walls, $\kappa = 2.0$				
$\tau_A = 5.125\mu s$				
a [m]	b [m]	a_w [m]	b_w [m]	b/b_w
0.5	1.00	1.80	2.00	0.5
		1.43	1.67	0.6
		1.14	1.43	0.7
		1.04	1.35	0.74
		0.97	1.30	0.77
		0.900	1.25	0.8
		0.694	1.11	0.9

Measured frequencies are summarized in table 4.2.

Given these data, $\omega^2\tau_A^2$ can be computed and final results are shown in Figure 4.8 for $\kappa = 2.0$ and in Figure 4.7 for $\kappa = 1.4$.

4.1.4 Self-similar wall scan, $\kappa = 2.0$

We now design self-similar walls. Again, data and measured frequencies are reported in table 4.3 and 4.4, respectively. The final plot of $\omega^2\tau_A^2$ is in Figure 4.9.

4.1.5 Elongation scan

Lastly, we want to evaluate the $\omega^2\tau_A^2$ as a function of parameter κ. For this scan, we keep the plasma current density constant at $J_p = 2{\times}10^{-5}$ A and also the value

Table 4.2: Frequencies and growth rates for confocal wall scans

Confocal walls, $\kappa = 1.4$		
b/b_w	**Frequency,** f **[kHz]**	**Growth rate,** γ
0.4		$47.6 \cdot 10^4$
0.5	1.50	
0.6	9.67	
0.7	15.3	
0.8	21.1	
0.83	25.0	
Confocal walls, $\kappa = 2.0$		
b/b_w	**Frequency,** f **[kHz]**	**Growth rate,** γ
0.5		$9.85 \cdot 10^4$
0.6		$8.36 \cdot 10^4$
0.7		$4.87 \cdot 10^4$
0.74	2.90	
0.77	7.99	
0.8	12.0	
0.9	14.7	

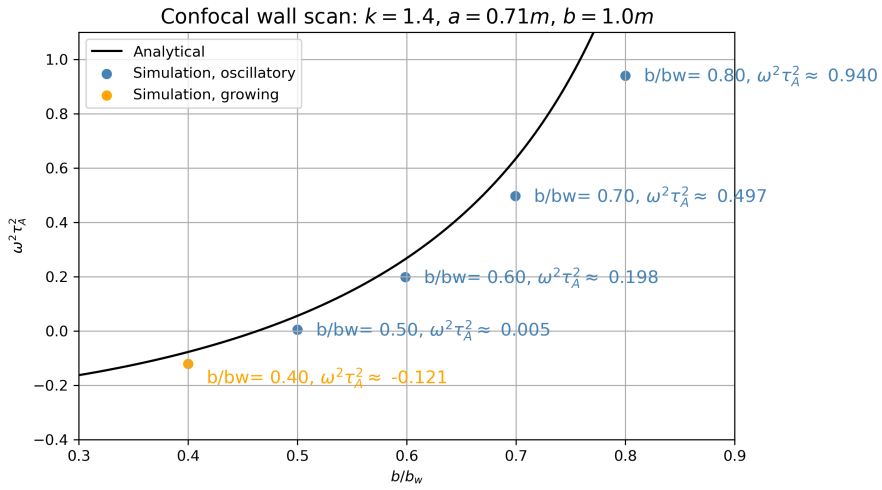

Figure 4.7: Confocal walls scan, $\kappa = 1.4$

$b/b_w = 0.25$ fixed.

Again, table 4.5 summarizes data and 4.6 reports measured frequencies and growth

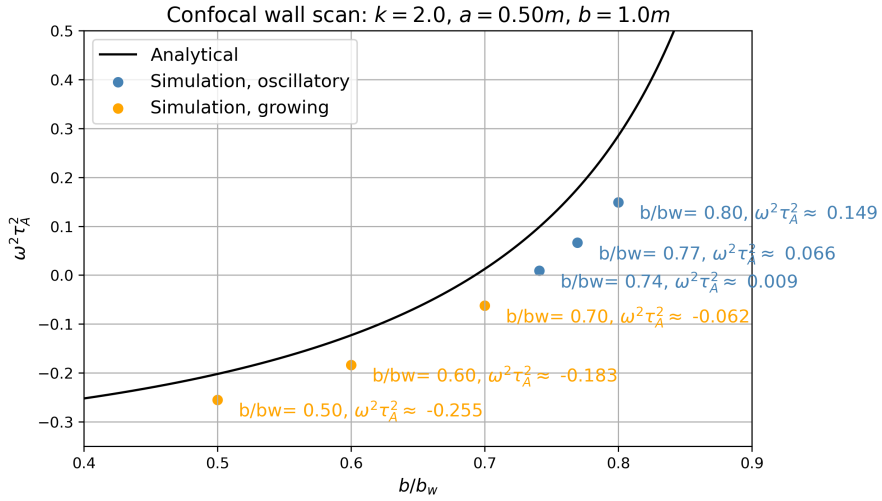

Figure 4.8: Confocal walls scan, $\kappa = 2.0$

Table 4.3: Data for self-similar walls scan

Self-similar walls scan, $\kappa = 2.0$				
$\tau_A = 5.125\mu s$				
a [m]	b [m]	a_w [m]	b_w [m]	b/b_w
0.5	1.00	0.833	1.67	0.6
		0.765	1.53	0.65
		0.745	1.49	0.67
		0.710	1.42	0.70
		0.680	1.36	0.74
		0.650	1.30	0.77

rates. Final plot is Figure 4.10.

4.1.6 Analysis

In previous Figures 4.7-4.9 the analytical function – represented by the solid lines – and the scattered points computed from the numerical simulations agree well, though there are no exact matches. The walls in the simulation form a rectangular boundary instead of the elliptical one of the analytical derivation, thus constituting a source of discrepancy between the two sets of data.

The rectangular wall is on average further away from the plasma than the equivalent

Table 4.4: Frequencies and growth rates for self-similar wall scan

Self-similar walls, $\kappa = 2.0$		
b/b_w	**Frequency,** f **[kHz]**	**Growth rate,** γ
0.6		$5.12 \cdot 10^4$
0.65		$4.65 \cdot 10^2$
0.67	5.00	
0.7	9.30	
0.74	12.2	
0.77	15.2	

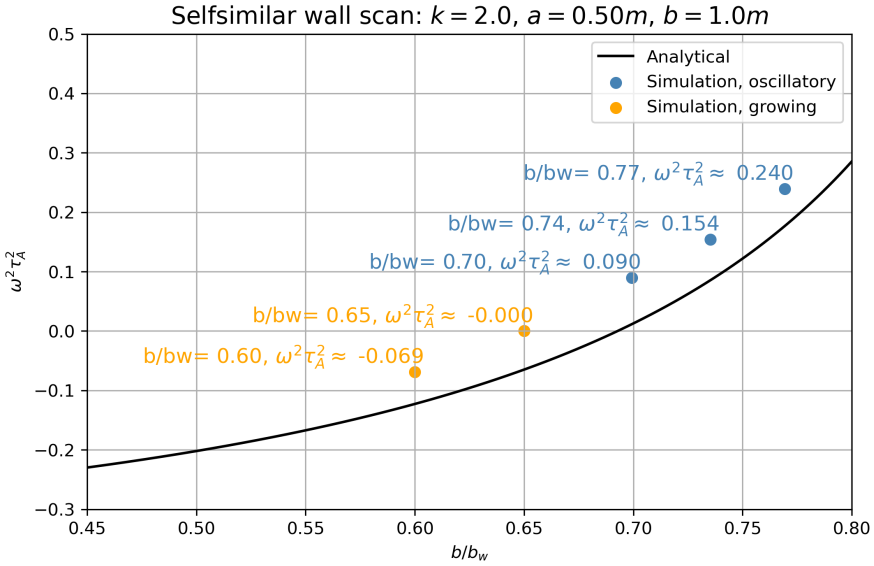

Figure 4.9: Self-similar walls scan, $\kappa = 2.0$

elliptical wall, as one could also notice in Figure 3.3. The stabilizing effect exerted by the rectangular wall is weaker and the growth rate is numerically a bit larger than analytically.

Notice how in the confocal wall scans, simulated dots lie below the analytical ones, contrary to the case of self-similar walls, where numerical simulation values lie above. This is indeed caused by the position of the walls, which is the only substantial difference between the two scans. The self-similarity condition positions the walls closer to the plasma with respect to the confocalilty condition. Refer to Figure 3.2 where this feature is clearly visible: the orange ellipses have the same b/a ratio as the black plasma ellipse, whereas the blue ones, which are confocal to

Table 4.5: Data for plasma elongation scan

Plasma elongation scan, $b/b_w = 0.25$					
$\tau_A = 5.125\mu s$					
a [m]	b [m]	a_w [m]	b_w [m]	κ	I_p[A]
0.990	1.00	3.96	4	1.01	$1.98 \cdot 10^5$
0.950	1.00	3.80	4	1.05	$1.90 \cdot 10^5$
0.910	1.00	3.64	4	1.10	$1.82 \cdot 10^5$
0.830	1.00	3.33	4	1.20	$1.66 \cdot 10^5$
0.769	1.00	3.08	4	1.30	$1.54 \cdot 10^5$

Table 4.6: Frequencies and growth rates for plasma elongation scan

Plasma elongation scan, $b/b_w = 0.25$		
κ	**Frequency,** f **[kHz]**	**Growth rate,** γ
1.01	9.67	
1.05	7.10	
1.10	2.89	
1.20		$5.23 \cdot 10^4$
1.30		$6.98 \cdot 10^4$

the black one, are noticeably further away from the plasma as the axes' dimension increases. The result is that, in the self-similar scan, the stabilizing effect of the wall is stronger with respect to what happens in the confocal scan.

4.1.7 Change to the density profile

A change of the density profile characteristics of the equilibrium produce differences in the frequency of oscillation of the simulated plasma.

Take the definition 3.6, which is also reported below for convenience:

$$n(\psi) = n_{halo} + (n_0 - n_{halo}) \frac{[1 - \tanh(\sigma(\psi - \psi_b)/\psi_b)]}{2} \tag{4.3}$$

The parameter σ controls the width of the hyperbolic tangent and thus the width of the transition from the density n_0 of the hot plasma region to the lower density of the halo plasma. The more narrow the transition, the more abrupt is the gradient

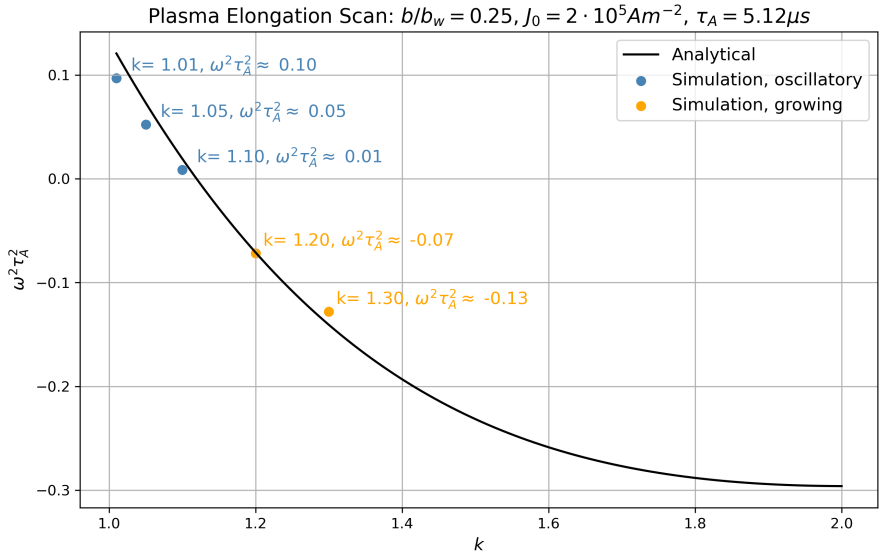

Figure 4.10: Plasma elongation scan, $b/b_w = 0.25$

and consequently the more complex is the simulation under a numerical point of view. For the linear simulations, this difference does not constitute a problem.

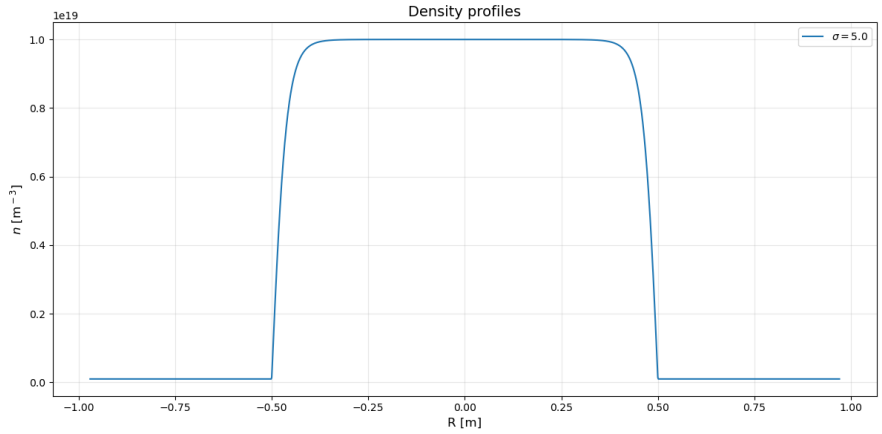

Figure 4.11: Density profile at the midplane $y = 0$ - $\sigma = 5.0$

In previous simulations, the density profile is the one represented in Figure 4.11. Figure 4.12a, instead, shows the two new profiles used for this test: one with larger σ and thus a sharper edge, and one with a lower value of σ and a broader transition.

The observed V_z for the two new cases are depicted in Figure 4.12b. The frequency of oscillation for the case with a broader transition increased, and viceversa for the

narrow transition, the frequency value is lower.

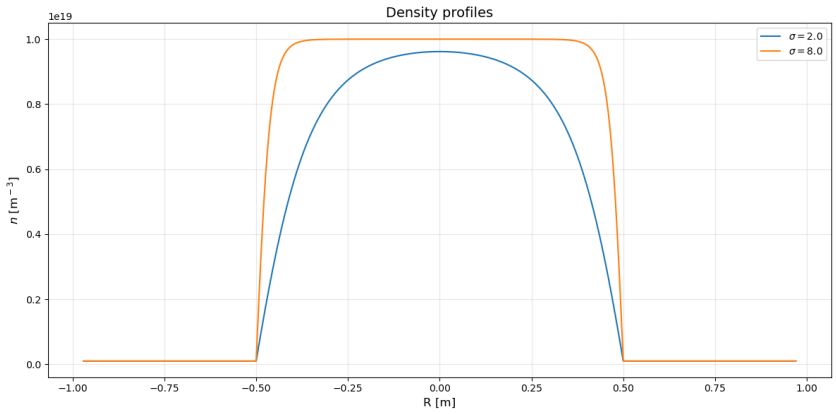

(a) Density profiles for different σ values. R represents the x-coordinate on a fixed $y = 0$

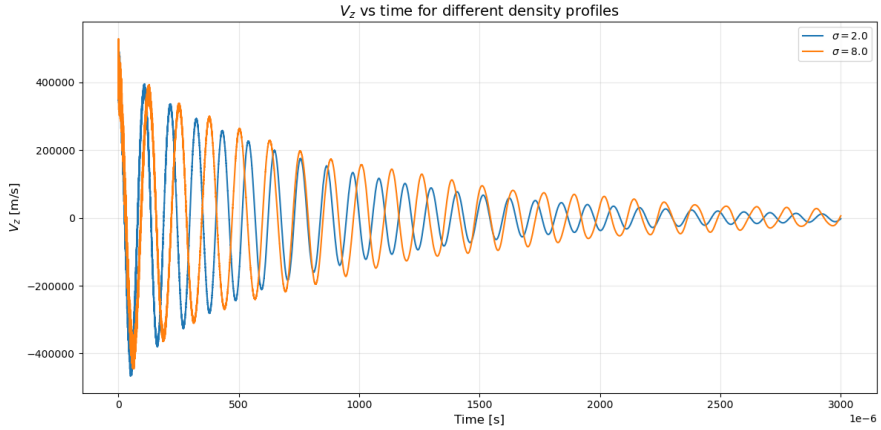

(b) $V_z(t)$ profiles for different σ values

Figure 4.12: Linear simulations with different density profiles at equilibrium

4.1.8 Midplane profiles of $V_z(t)$

Most of the plots in this chapter represent the time evolutions of the quantity V_z, probed in a position in the hot plasma region which stays fixed throughout the simulation. Figure 4.13, instead, represents evolutions in space: each line in the plot shows the value of V_z across the midplane, $y = 0$, of the domain at a fixed instant of time. All together they span one period of oscillation of the VDOM, specifically, from $\sim$ 1 ms to $\sim$ 1.06 ms for the case of "confocal walls, $\kappa = 1.4$,

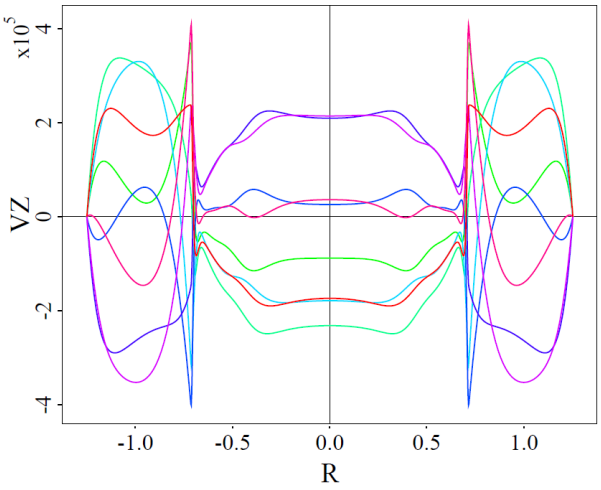

Figure 4.13: V_z as a function of space. Coordinate R represents the x-coordinate at fixed $y = 0$. Each color represents the profile of the vertical velocity at a different time stamp.

$b/b_w = 0.7"$.

The structure of this profiles shows how the $n = 0$ oscillations are confined to the hot plasma region (up to $R = 0.71$ for this example). Outside of this region a return flow is carried by the halo plasma. It contributes to satisfy the incompressibility condition, but it is small compared to the mass flow in the hot plasma.

4.2 Linear simulation with driven oscillator perturbation

To study the oscillatory modes found in the previous section, a useful tool is implemented in the NIMROD code. Previously, simulations used an initial vertical push of finite amplitude, and a FFT analysis revealed multiple frequencies of oscillations. We are now interested in isolating the VDOM solution. For this reason it is necessary to modify the temperature evolution equation, in order to include an additional time-dependent oscillatory term:

$$\frac{3}{2}\left(\frac{\partial}{\partial t} + \vec{v}\cdot\nabla\right) T = -nT\nabla\cdot\vec{v} + A\sin\left(2\pi f_0 t\right)\exp\left(\frac{(r-r_0)^2 + (z-z_0)^2}{\Delta_0^2}\right) \quad (4.4)$$

In this expression, f_0 is the driven oscillation frequency for the temperature, A is the amplitude of the driving term. The oscillatory perturbation is localized as

a Gaussian function of width Δ_0 at poloidal coordinates (r_0, z_0). All other fields have vanishing initial perturbation.

Overall the effect of adding this term is forcing in the plasma a resonant response associated to the plasma normal modes that we are interested in. Thanks to it, we are able to isolate the frequency of the VDOM and confirm the data of the FFT.

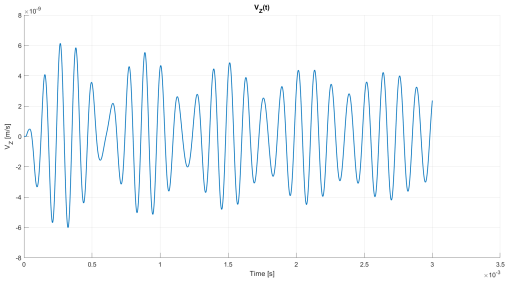

(a) $f_0 = 8.00$ kHz - maximum amplitude of the oscillation $\sim 6.0 \cdot 10^{-9}$ m/s

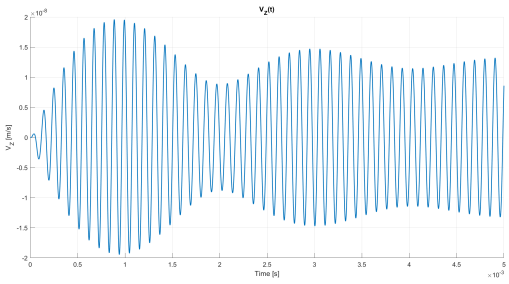

(b) $f_0 = 9.20$ kHz - maximum amplitude of the oscillation $\sim 2.0 \cdot 10^{-8}$ m/s

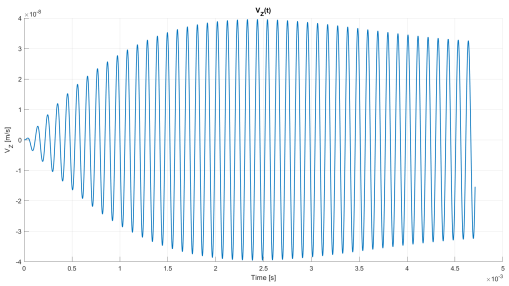

(c) $f_0 = 9.52$ kHz - maximum amplitude of the oscillation $\sim 4.0 \cdot 10^{-8}$ m/s

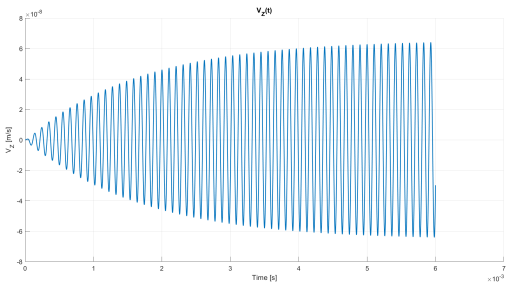

(d) $f_0 = 9.67$ kHz - maximum amplitude of the oscillation $\sim 6.0 \cdot 10^{-8}$ m/s

Figure 4.14: Plots for progressively increasing frequency f_0 of the forcing term on the case with confocal walls, $\kappa = 1.4$ and $b/b_w = 0.6$

In Figure 4.14 the behaviour of V_z when applying the forcing temperature term is shown: 4.14d represents the resonance; 4.14a, 4.14b, 4.14c are off-resonance.

When the oscillator resonates with the mode, a growing oscillatory pattern is observed. The envelope of the oscillation grows and eventually saturates over time.

For the case where the forcing term is not set at the right frequency, it is clearly observable a beating frequency $f_b = |f - f_0|$ where f_0 is the oscillator frequency and f is the mode frequency. Eventually as time grows, the beating fades away and the constant amplitude oscillation at the forcing frequency is left.

One may decide to perform a scan in the forcing perturbation frequency: modifying the oscillator frequency in the neighbourhood of the VDOM frequency changes the

amplitude of the output oscillations measured at saturation. Figure 4.15 plots the data of the maximum amplitudes of the V_z field when forced at certain frequencies. The data points are fitted by a Lorentzian function $C/\left(\sqrt{(\omega_0-\omega)^2+\gamma^2}\right)$, where C is a constant, ω and γ are related to the peak and width of the function, and ω_0 is the frequency of the forcing term.

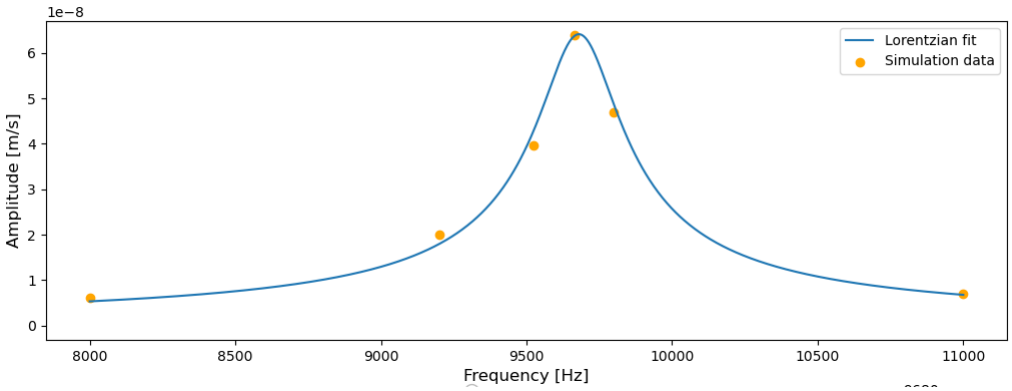

Figure 4.15: Data points for the maximum amplitude of V_z on simulations with driven oscillator perturbation as a function of frequency f_0

4.3 Nonlinear simulations

Nonlinear simulations require more attention than their linear counterparts. Especially from a computational point of view, every input parameter may determine if the simulations encounters numerical problems or if it runs smoothly. Moreover, numerical simulations are significantly more complex requiring more time and more computational resources. These are the reasons why it was necessary to modify the input values with respect to the ones used for the linear simulations. Most of the nonlinear simulated cases also ran for a significantly shorter simulation time than the linear counterparts, as it would have been otherwise too time consuming.

4.3.1 Motivation for nonlinear analysis

Linear simulations are able to reproduce analytical results, but this is not sufficient. Since the linear model describes the evolution of the system under infinitesimal perturbations, there is a wide range of phenomena and dynamics which do not appear in linearized equations, and for instance a system might be unstable to perturbations above a certain threshold. A nonlinear numerical approach becomes

necessary to understand the evolution of the system in its entirety.

We advance here the hypothesis that even though through a linear analysis the VDOM appear stable, under specific conditions, these same cases might become unstable when accounting for nonlinearity. In particular, we believe that we should focus on conditions near the marginal stability.

4.3.2 Finite amplitude perturbations

Nonlinear simulations were designed to test the different behaviour of the plasma when stepwise increasing the amplitude of the initial perturbation. This is designed as for the liner simulations as a vertical push whose value is specified as $\tilde{B}$, the perturbed magnetic field.

Linear cases from the previous sections were chosen and reanalyzed: for example, one is *confocal walls,* $\kappa = 2.0$*, and* $b/b_w = 0.9$, which had a VDOM frequency of $1.47{\times}10^4$ Hz, easier to observe on shorter time ranges; other cases are instead conveniently close to the marginal stability condition, $\omega = 0$.

The amplitude of the initial perturbation starts at 10^{-5} T and increases up to 10^{-2} T.For the nonlinearity aspect to impact the results, values of V_z should reach orders of 10^5 m/s. For this to happen, the amplitude of the initial perturbation must be in the order of 10^{-2} T.

In Figure 4.16 one can observe for the case further from the marginal stability condition the evolution in time of the V_z field. Larger initial perturbation amplitude results in the increase by a corresponding amount of the output. For comparison, Subfigure 4.16d shows the linear evolution of the same case with an initial perturbation amplitude of $\tilde{B} = 10^{-4}$ T: even though it shows a much longer simulation, it matches the nonlinear evolution almost exactly, within the nonlinear simulation time frame. Subtle changes in the shape of the oscillations were observed when increasing this value, but most of the difference is observed in the contour plots. Observe Figure 4.17. It shows the contour plots of the perturbed pressure $\tilde{p}$ for a non linear simulation with a small amplitude of initial vertical push. It reproduces the behaviour observed in linear stable cases, since the initial perturbation is $\tilde{B} = 10^{-3}$ T. Each contour plot is taken at certain time stamps during the simulation. The structure of the oscillation is recognizable.

Figure 4.18 shows the contour plots for the pressure field for a nonlinear simulation with initial vertical push $\tilde{B} = 10^{-2}$ T. This is above the threshold for nonlinear effects. Plots on each row are taken at the same time stamp throughout the simulation. Plots in the left column only show $\tilde{p}$, whereas in the column on the right the total pressure field is plotted, comprehensive of both the equilibrium value

Figure 4.16: Case *confocal walls*, $\kappa = 2.0$ *and* $b/b_w = 0.9$

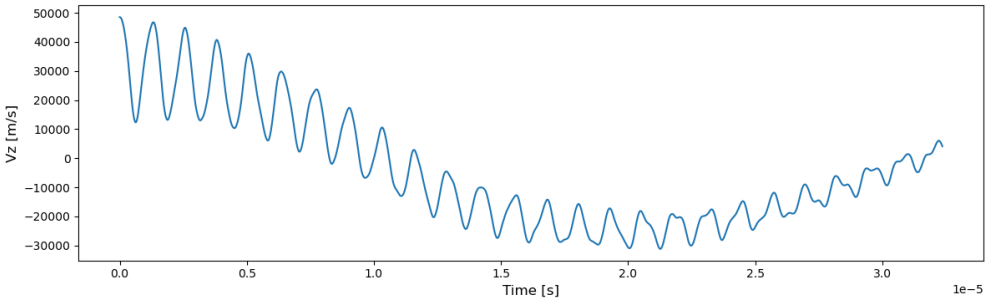

(a) Initial amplitude $\tilde{B} = 10^{-2}\,\mathrm{T}$

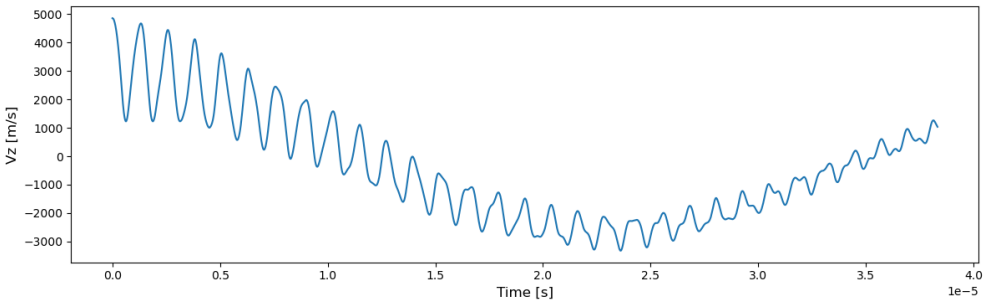

(b) Initial amplitude $\tilde{B} = 10^{-3}\,\mathrm{T}$

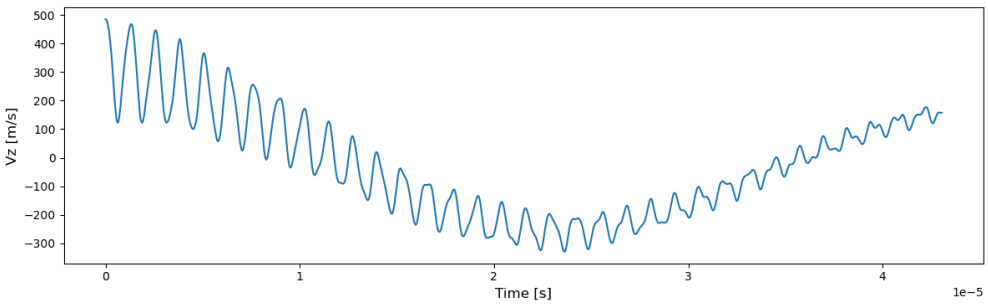

(c) Initial amplitude $\tilde{B} = 10^{-4}\,\mathrm{T}$

Figure 4.16: Case *confocal walls*, $\kappa = 2.0$ *and* $b/b_w = 0.9$

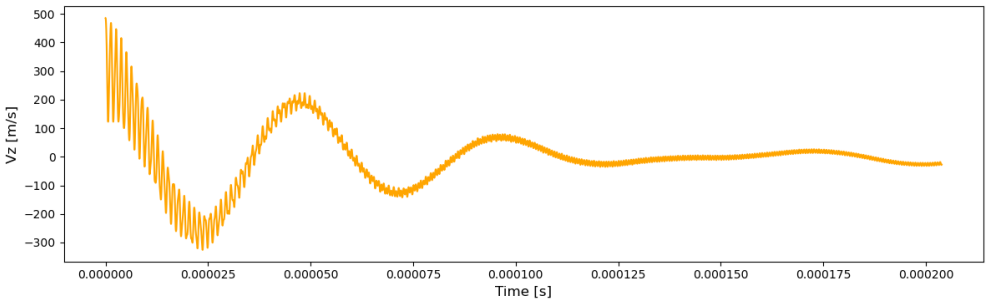

(d) Linear case - initial amplitude $\tilde{B} = 10^{-4}\,\mathrm{T}$

p_0 and the perturbation $\tilde{p}$.

A vertical displacement of the plasma can be noticed: the elliptical shape of the plasma in the center of the plots, moves in the positive direction of Z and starts an oscillation about the equilibrium position. This is also confirmed by how the V_z field behaves in plot 4.16a. The motion is clearer in the total pressure field contour plots. The vertical displacement is small, but it is present, contrary to the linear cases, where the resulting behaviour was independent of the initial vertical perturbation amplitude: an increase in this quantity only reflected in a linear increase in the total amplitude of the resulting fields, but no real displacement could be seen.

Simulation near the marginal stability have shown the same behaviour. Figures 4.19 and 4.20 show two of this cases: the first depicts half an oscillation of the perturbed pressure field; the latter shows the total pressure field. Both sets of plots show clearly the vertical displacement of the plasma with respect to its equilibrium position and a related deformation of the ellipitcal equilibrium shape.

4.3.3 Evolving the equilibrium

In section 3.3, it was briefly mentioned how the simulations preserve the equilibrium. This might not be true for nonlinear simulations. Originally added to help against numerical errors, the NIMROD code for nonlinear cases features the possibility of advancing in time the total quantities, sum of the perturbations and the equilibrium values. This makes the simulation more realistic.

To check if the already discussed equilibrium configuration is stable in the nonlinear phase, we perform a simulation that has no initial perturbation. It behaves as in

Figure 4.17: Nonlinear simulations for *confocal walls*, $\kappa = 2.0$, $b/b_w = 0.9$, and $\tilde{B} = 10^{-3}$ T: contour plots of the pressure field $\tilde{p}$

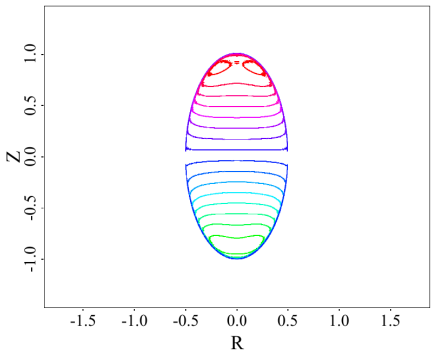

(a) $t = 0\mu s$

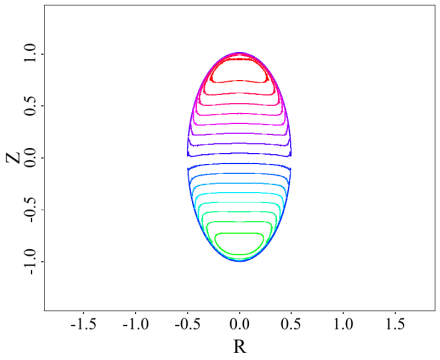

(b) $t = 4.0\mu s$

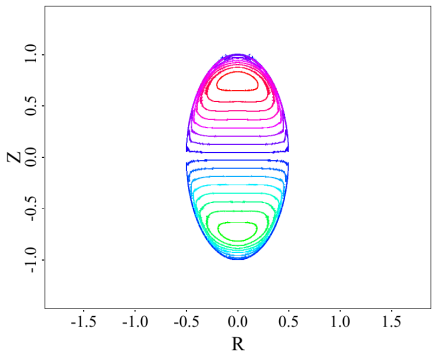

(c) $t = 11\mu s$

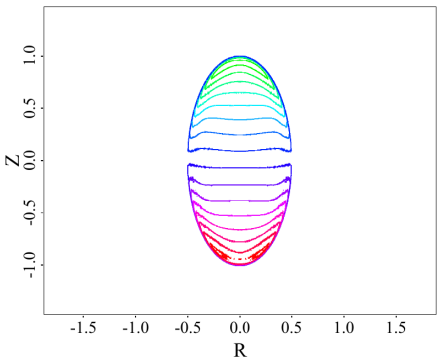

(d) $t = 20\mu s$

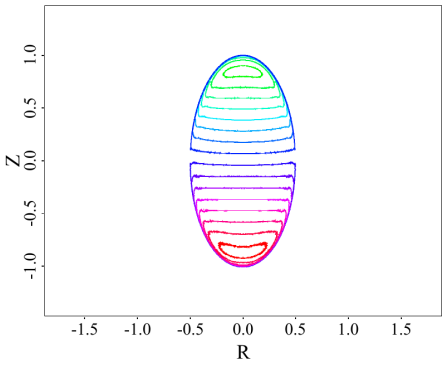

(e) $t = 30\mu s$

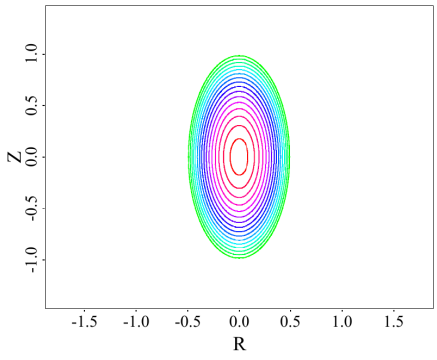

(f) Total pressure field, at $t = 0\mu s$

Figure 4.18: Case of confocal walls, $\kappa = 2.0$, $b/b_w = 0.9$, and $\tilde{B} = 10^{-2}\,\mathrm{T}$: nonlinear contour plots of pressure p. On the left plots represent the perturbation; the quantity plotted on the right is the total pressure (equilibrium + perturbation)

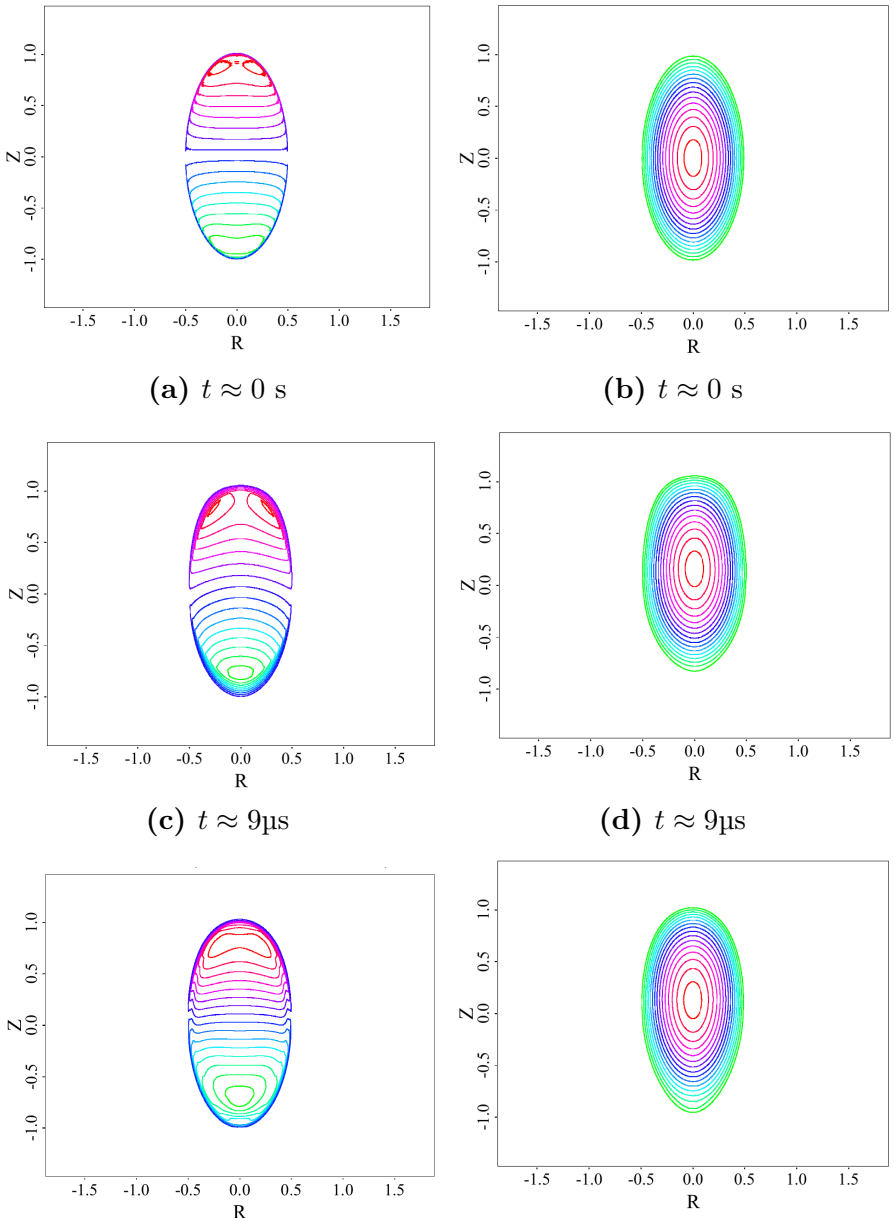

(a) $t \approx 0$ s **(b)** $t \approx 0$ s

(c) $t \approx 9\mu$s **(d)** $t \approx 9\mu$s

(e) $t \approx 15\mu$s **(f)** $t \approx 15\mu$s

Figure 4.18: Case of confocal walls, $\kappa = 2.0$, $b/b_w = 0.9$, and $\tilde{B} = 10^{-2}\,\mathrm{T}$: nonlinear contour plots of pressure p (continued)

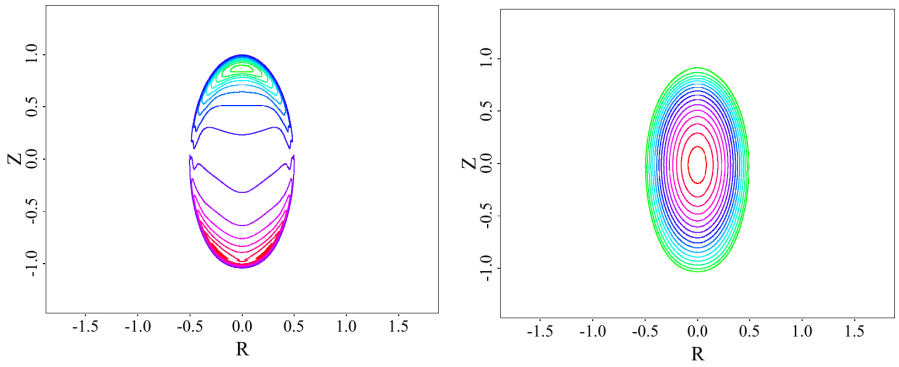

(g) $t \approx 25\mu\mathrm{s}$

(h) $t \approx 25\mu\mathrm{s}$

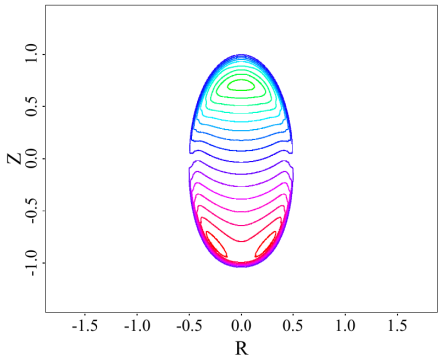

(i) $t \approx 35\mu\mathrm{s}$

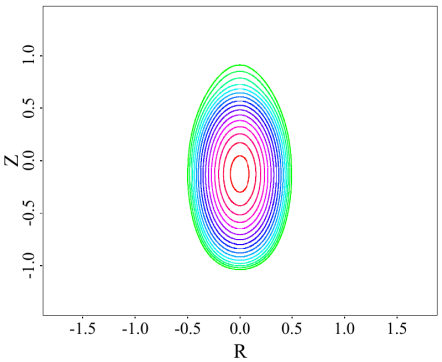

(j) $t \approx 35\mu\mathrm{s}$

Figure 4.19: Nonlinear simulation of confocal walls, $\kappa = 1.4$, $b/b_w = 0.72$, and $\tilde{B} = 3{\times}10^{-2}$ T: contour plots of $\tilde{p}$

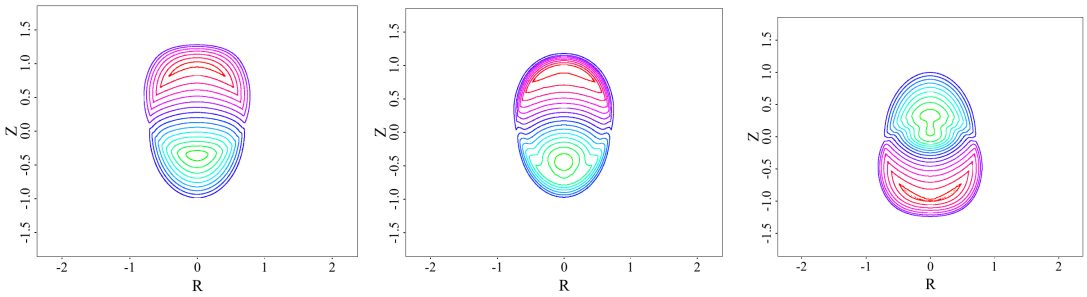

(a) **(b)** **(c)**

Figure 4.20: Nonlinear simulation of confocal walls, $\kappa = 2.0$, $b/b_w = 0.74$, and $\tilde{B} = 3{\times}10^{-2}$ T: contour plots of p

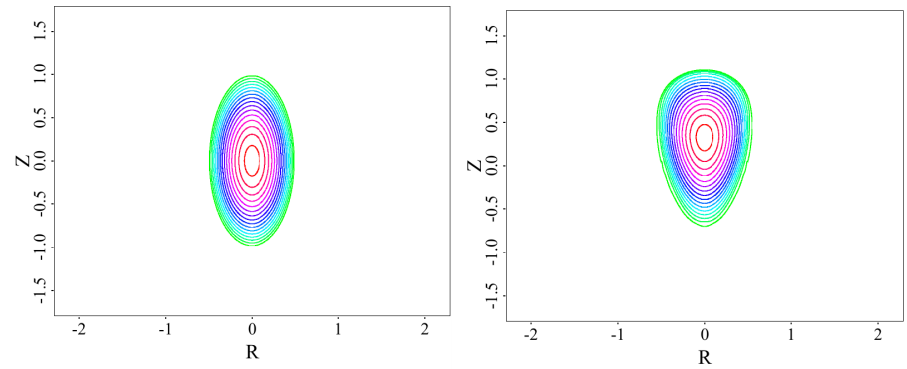

(a) Equilibrium **(b)**

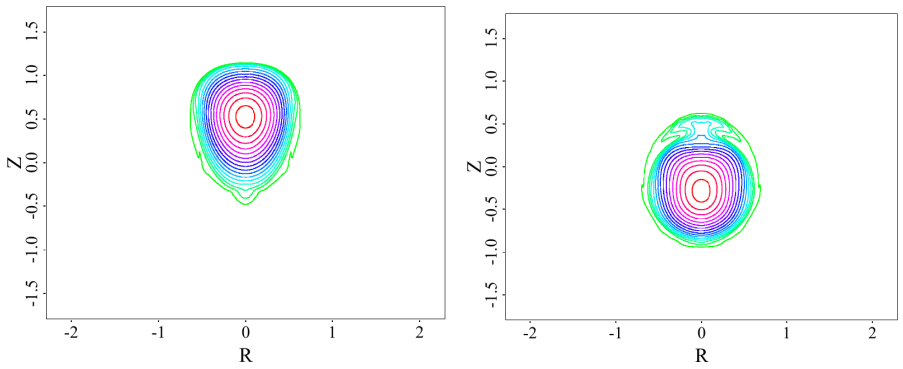

(c) **(d)**

Figure 4.21, where the vertical component of the velocity oscillates at a frequency ~ 60 kHz. This oscillation can be interpreted as a relaxation of the equilibrium due to diffusivity.

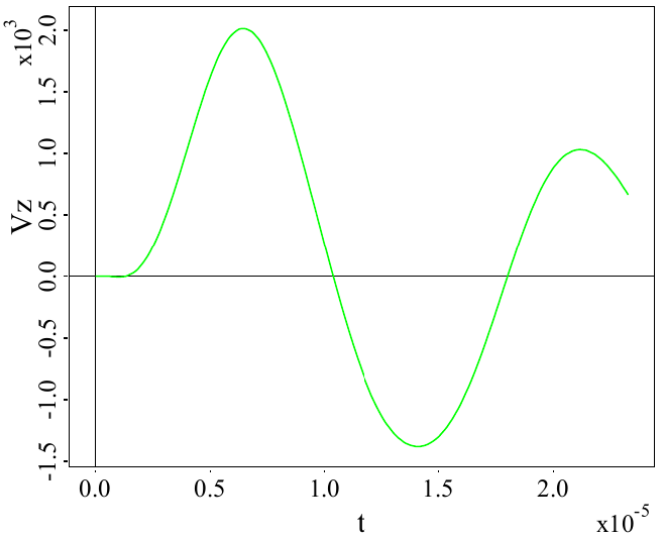

Figure 4.21: Observed oscillation for $\tilde{B} = 0$ when NIMROD evolves the equilibrium values

In these conditions, the dynamics of the VDOM are hidden by the relaxation of the equilibrium if we do not provide an initial perturbation value sufficiently high to produce large enough $V_z > 10^3\,\mathrm{m/s}$.

Chapter 5

Conclusions and future work

This thesis has provided analytical and numerical results on axisymmetric modes in tokamaks. Understanding these type of instabilities is a step forward towards the improvement of the safety and the performance of tokamak devices.

Modern day tokamaks with non-circular cross sections, where both the plasma shape and that of the confining walls of the vacuum chamber are elongated, have the important advantage of increased instability thresholds in terms of toroidal plasma current and beta values against ideal magnetohydrodynamic (MHD) modes. Unfortunately, elongation is also closely related to the insurgence of an instability initiated by an axisymmetric perturbation with toroidal mode number $n = 0$. These instabilities potentially lead to vertical displacement events (VDEs), which are dangerous to the mechanical structure of the device. Starting from the ideal MHD model, where dissipative phenomena are neglected, Chapter 2 derives the dispersion relation for these vertical displacement normal modes. The relevant expression has two solutions in the ideal wall case or three for the resistive wall case. In the latter scenario, a purely growing mode with zero frequency emerges. This mode is suppressed by active feedback control systems in tokamak experiments. The two other roots are typically referred to as *vertical displacement oscillatory modes* (VDOMs) and they are purely oscillatory for the ideal wall case.

Numerical simulations performed using the NIMROD code in this thesis aimed at exploring the characteristics of these modes.

A first set of simulations is performed with the intention of solving the linearized version of the ideal MHD model, as described in Chapter 3. The linear analytical theory, provides a relation for the frequency ω of oscillation of the modes as a function of the geometric characteristics of the system. Each simulation is designed by perturbing the equilibrium configuration of the plasma with a small finite

amplitude vertical shift in the magnetic field. This type of perturbation is adopted because it resembles the VDOM eigenfunction. The VDOM structure, indeed, corresponds to a rigid vertical shift of the plasma column. We are interested in the time evolution of the system and we focus on the quantity V_z, vertical component of the velocity. Three are the parameters that change in the simulations: shape of the plasma, namely its elongation, the distance between the boundary of the plasma region and the wall, and the shape of the walls with respect to that of the plasma, i.e. dimensions of the walls can be set according to a confocality or self similarity condition. All linear simulations reproduce the theory associated to them.

The frequency ω grows as the walls get closer to the plasma. This behaviour is observed in the simulations: as the walls move away from the plasma, the stabilization effect they have on the modes grows weaker until what is observed are unstable growing oscillations. Moreover, the frequency of oscillation of the VDOMs decreases as the elongation of the plasma grows. This is also observed, until a certain critical value after which oscillations grow unstable. This transition from stable to unstable corresponds to the criterion when the boundary of the walls intersects the X-points of the magnetic configuration of the plasma. It takes the name of marginal stability. All of these behaviours are in good agreement with the analytical theory of VDOMs. There are some small discrepancies, but they are readily explained: the main difference with the analytical model is that the confocal ellipse of the wall is substituted in the simulation by a rectangular boundary. This modification reflects on the simulated frequencies, which do not reproduce exactly the analytical values, but slightly higher or lower values.

Until this point, the perturbation of the equilibrium configuration of the plasma was an initial finite amplitude vertical shift. This type of perturbation simulates the type of eigenfunctions which are associated to the $n = 0$, $m = 1$ modes. Nonetheless, the system evolution does not show only the VDOMs structure, and the response is more complex, as shown by the Fast Fourier Transform analysis. For this reason, it is convenient to introduce in the temperature equation a forcing term, which we have called driven oscillator perturbation. Its effect is prompting the plasma to a resonant response associated to the VDOMs. By setting the frequency of the forcing term oscillation to the VDOM frequency, we are able to isolate the mode.

All these linear results constitute a solid basis and prompt future investigation with the idea of implementing in the simulation more accurate geometries and different equilibrium configurations.

The innovative approach of this thesis to the study of VDOMs consists in performing nonlinear simulations, prompted by the difficulty to explicitly derive mathematical expressions for these cases. Though the results presented in this thesis only scratch

the surface of this topic, they lay the basis for future works. The idea behind the investigation of nonlinearity comes from the hypothesis that linearly stable oscillations might be nonlinearly unstable. For this reason, this thesis aimed at performing nonlinear simulations on cases which, after the linear analysis, appeared close to the marginal stability, $\omega = 0$, but still on the stable side, $\omega^2 > 0$. Working with these cases requires a lot of computational resources, because of the low frequency at which they oscillate. This is why the analysis was performed first on a case which was farther away from the marginal stability. The plasma equilibrium configuration is perturbed by a small vertical shift. The behaviour of the vertical component of the velocity that we observe evolves in time according the ideal MHD model. The simulations was more noisy with respect their linear counterparts because of the necessity to change some of the simulating parameters such as electrical diffusivity and the viscosity properties of the plasma. Still, the oscillation matches that of the linear case. We then test how the behaviour changes when the amplitude of the initial perturbation grows. When it becomes sufficiently high, observing the plasma pressure field evolution in time reveals a nonlinear effect: the plasma column shifts vertically inside the walls. This displacement continues in time as an oscillation. Qualitatively this behaviour is found in the analysis of multiple cases whose VDOM oscillated at different frequencies.

In the context of nonlinear analysis, this thesis introduces a topic related to a specific feature of the NIMROD code. In all linear simulations, the equilibrium configuration was fixed in time. In the nonlinear cases, the equilibrium values can be evolved together with the perturbation. In this way, one finds a oscillation in time representing the relaxation of the equilibrium due to the effects of diffusivity. This influences the evolution of VDOM modes, especially for the cases in which the initial vertical perturbation has small amplitude. Further work on this aspect of nonlinear simulation must be done.

Future investigation is needed to fully grasp the range of the nonlinear effects on tokamak plasmas. One of the topics it should focus on is, for example, the possibility of applying the driven oscillator perturbation method to the nonlinear cases, as it was done on the linear ones. This might open a new road to understanding the nonlinear behaviour of VDOMS.

In conclusion, linear numerical results presented in this thesis confirm the validity of the theoretical work. Nonlinear simulations, instead, constitute ground basis for future applications of the NIMROD code on the study of VDOMs in tokamak plasmas.

Bibliography

[1] International Energy Agency. *Energy and AI*. Tech. rep. Licence: CC BY 4.0. Paris: International Energy Agency, 2025. URL: https://www.iea.org/reports/energy-and-ai (cit. on p. 1).

[2] C. Bustreo et al. «Socio economic perspectives on fusion power for a sustainable future energy system». In: *Fusion Engineering and Design* 208 (2024), p. 114679. ISSN: 0920-3796. DOI: https://doi.org/10.1016/j.fusengdes.2024.114679. URL: https://www.sciencedirect.com/science/article/pii/S0920379624005301 (cit. on p. 1).

[3] J D Lawson. «Some Criteria for a Power Producing Thermonuclear Reactor». In: *Proceedings of the Physical Society. Section B* 70.1 (Jan. 1957), p. 6. DOI: 10.1088/0370-1301/70/1/303. URL: https://doi.org/10.1088/0370-1301/70/1/303 (cit. on p. 3).

[4] V.P. Smirnov. «Tokamak foundation in USSR/Russia 1950–1990». In: *Nuclear Fusion* 50.1 (Dec. 2009), p. 014003. DOI: 10.1088/0029-5515/50/1/014003. URL: https://doi.org/10.1088/0029-5515/50/1/014003 (cit. on p. 5).

[5] Guido Van Oost, Sehila M. Gonzalez de Vicente, et al., eds. *Fundamentals of Magnetic Fusion Technology*. Includes chapter "Introduction to Magnetic Fusion and Fusion Reactors", accessed: 2026-02-17. Vienna, Austria: International Atomic Energy Agency, 2023. ISBN: 978-92-0-110721-3. URL: https://www.iaea.org/publications/14898/fundamentals-of-magnetic-fusion-technology (cit. on p. 5).

[6] Jeronimo Garcia et al. «Stable Deuterium-Tritium plasmas with improved confinement in the presence of energetic-ion instabilities». In: *Nature Communications* 15 (2024), p. 7846. DOI: 10.1038/s41467-024-52182-z. URL: https://doi.org/10.1038/s41467-024-52182-z (cit. on p. 5).

[7] ITER Organization. *ITER – International Thermonuclear Experimental Reactor*. Accessed: 2026-02-17. ITER Organization. 2026. URL: https://www.iter.org/ (cit. on pp. 5, 16).

[8] Max Planck Institute for Plasma Physics. *Stellarator*. Accessed: 2026-03-12. n.d. URL: https://www.ipp.mpg.de/14779/stellarator (cit. on p. 6).

[9] ENN Energy Research Institute. *EXL-50 Spherical Torus Fusion Device*. Compact fusion research page describing the EXL-50 experimental device. Accessed: 2026-03-14. 2020. URL: https://en.ennresearch.com/research field/Compactfusion/device/ (cit. on p. 6).

[10] UK Atomic Energy Authority. *MAST Upgrade: The world's largest operational spherical tokamak*. Accessed: 2026-03-14. n.d. URL: https://www.ukaea.org/work/mast-upgrade/ (cit. on p. 6).

[11] Bruno Coppi. «A high magnetic field compact tokamak approach to ignition». In: *Comments on Plasma Physics and Controlled Fusion* 3 (1977), pp. 47–53 (cit. on p. 7).

[12] Guy Laval, James D. Callen, Geoffrey Cordey, Otto Gruber, Wendell Horton, Jean Jacquinot, Jean-Francois Luciani, and Franco Porcelli. *Thermonuclear Tokamak Panel Report*. Tech. rep. Panel convened by R. Pellat, High Commissioner of CEA, to evaluate the physics basis of the ITER-FEAT and IGNITOR proposals; meeting held 25–26 November 1999. Paris, France: Commissariat à l'Énergie Atomique (CEA), Nov. 1999. URL: https://fire.pppl.gov/pellat_panel_final.pdf.pdf (cit. on p. 7).

[13] MIT Plasma Science and Fusion Center. *SPARC*. Accessed: 2026-03-12. n.d. URL: http://www-new.psfc.mit.edu/sparc (cit. on p. 7).

[14] CFS/MIT-PSFC. *Cutaway rendering of the SPARC tokamak*. CAD rendering by T. Henderson, published on MIT News. Accessed: 2026-03-14. 2020. URL: https://news.mit.edu/2020/physics-fusion-studies-0929 (cit. on p. 7).

[15] T. Barberis, F. Porcelli, and A. Yolbarsop. «Fast-ion-driven vertical modes in magnetically confined toroidal plasmas». In: *Nuclear Fusion* 62.6 (Apr. 2022), p. 064002. DOI: 10.1088/1741-4326/ac5ad0. URL: https://doi.org/10.1088/1741-4326/ac5ad0 (cit. on p. 8).

[16] H. R. Strauss. «Nonlinear, three-dimensional magnetohydrodynamics of noncircular tokamaks». In: *Physics of Fluids* 19.1 (1976), pp. 134–140. DOI: 10.1063/1.861310 (cit. on p. 15).

[17] Francesco Romanelli. «Il progetto DTT». In: *ENEA EAI - Energia, Ambiente e Innovazione* (2023). DOI: 10.12910/EAI2023-062. URL: https://www.eai.enea.it/nuovo-nucleare-ricerca-tecnologie-scenari-e-prospettive/nuovo-nucleare-scenari/il-progetto-dtt.html (cit. on p. 18).

[18] F. Porcelli and A. Yolbarsop. «Analytic equilibrium of "straight tokamak" plasma bounded by a magnetic separatrix». In: *Physics of Plasmas* 26.5 (2019), p. 054501. DOI: 10.1063/1.5096838 (cit. on pp. 21, 23).

[19] G. Laval, R. Pellat, and J. L. Soule. «Hydromagnetic stability of a current-carrying pinch with noncircular cross section». In: *Physics of Fluids* 17.4 (1974), pp. 835–845. DOI: 10.1063/1.1694796 (cit. on p. 21).

[20] A. Yolbarsop, F. Porcelli, and R. Fitzpatrick. «Impact of magnetic X-points on the vertical stability of tokamak plasmas». In: *Nuclear Fusion* 61.11 (2021), p. 116042. DOI: 10.1088/1741-4326/ac1f4f (cit. on p. 22).

[21] A. Yolbarsop, F. Porcelli, W. Liu, and R. Fitzpatrick. «Analytic theory of ideal-MHD vertical displacements in tokamak plasmas». In: *Plasma Physics and Controlled Fusion* 64.10 (2022), p. 105010. DOI: 10.1088/1361-6587/ac8e16 (cit. on p. 22).

[22] F. Porcelli, A. Yolbarsop, T. Barberis, and R. Fitzpatrick. «Resonant Axisymmetric Modes». In: *Journal of Physics: Conference Series* 2089.1 (2021), p. 012041. DOI: 10.1088/1742-6596/2089/1/012041 (cit. on p. 22).

[23] I. B. Bernstein, E. A. Frieman, M. D. Kruskal, and R. M. Kulsrud. «An energy principle for hydromagnetic stability problems». In: *Proceedings of the Royal Society A* 244 (1958), pp. 17–40. DOI: 10.1098/rspa.1958.0029 (cit. on p. 24).

[24] A H Glasser, C R Sovinec, R A Nebel, T A Gianakon, S J Plimpton, M S Chu, D D Schnack, and the NIMROD Team. «The NIMROD code: a new approach to numerical plasma physics». In: *Plasma Physics and Controlled Fusion* 41.3A (Mar. 1999), A747. DOI: 10.1088/0741-3335/41/3A/067. URL: https://doi.org/10.1088/0741-3335/41/3A/067 (cit. on p. 32).

[25] *NIMROD Magnetohydrodynamic Code Team Homepage*. Accessed: 2026-02-16. The NIMROD Team. 2026. URL: https://nimrodteam.org/ (cit. on p. 32).

[26] CINECA HPC Documentation. *Pitagora — CINECA HPC Documentation*. Accessed: 2026-02-16. CINECA Documentation. 2026. URL: https://docs.hpc.cineca.it/hpc/pitagora.html (cit. on p. 33).